Wave Pattern Analysis for the Determination of Wave-Induced Resistance and Side Forces

Extending the Transverse Wave Cut Method to Side Forces

Joris Krämer

Delft University of Technology

TU Delft

Wave Pattern Analysis for the Determination of Wave-Induced Resistance and Side Forces

Extending the Transverse Wave Cut Method to Side Forces

by

Joris Krämer

Thesis for the degree of MSc in Marine Technology in the specialization of Ship Hydromechanics

at the Delft University of Technology,

to be defended publicly on Thursday, June 4, 2026, at 14:15.

Student number:	5167353		
Report number:	MT.25/26.031.M		
Project duration:	September, 2025 – June, 2026		
Cover image:	H-Boat, Rotterdam 2026 – photograph by the author		
Thesis committee:	*Chair*	Prof. G.D. Weymouth	Ship Hydrodynamics
	Member	Dr. ir. H.J. de Koning Gans	Ship Hydrodynamics
	Member	Dr. ir. J.O. Colomes Gene	Offshore Engineering

An electronic version of this thesis is available at `http://repository.tudelft.nl/`.

During the preparation of this work, AI tools were used only for language improvement, proofreading, and general assistance. The author bears full responsibility for the content of this work.

TU Delft

Preface

This thesis was written as a part of the Marine Technology MSc program at the TU Delft, in the section Ship Hydrodynamics.

During my BSc final project, my teammates and I worked on generating ship hulls using a single source and sink distribution, which we then simulated and tested with a panel method. We found that for slender, pointy hulls, the predicted resistance force would return a negative value. Rather than assuming that we had discovered a hull behaving as a *perpetuum mobile*, we investigated the force prediction method more closely. It turned out that the pressure integration method does not always return accurate answers under certain conditions. Our supervisor, Henk de Koning Gans, then introduced me to an alternative for calculating the resistance force: wave pattern analysis.

In the MSc course *Numerical Ship Hydrodynamics*, taught by Gabe Weymouth, I applied wave pattern analysis for the first time to calculate the wave resistance. I calculated integral equations for a wave cut behind the ship, using the flow field from a panel method. Unfortunately, the results were not consistent for different locations, and I was not able to solve it.

This experience was the inspiration for this master's thesis. I was fortunate that both Gabe Weymouth and Henk de Koning Gans, who helped and inspired me during these earlier projects, agreed to supervise the work. This thesis aims to further investigate wave pattern analysis as a method for predicting wave resistance and side force, and to assess its consistency and applicability for panel methods and CFD simulations.

The completion of this thesis would not have been possible without the help of my supervisors and committee members. I would like to thank Henk de Koning Gans for his constant availability and, in particular, for always taking the time to help me, even when I showed up unannounced with questions. I would also like to thank Gabe Weymouth for his helpful feedback and his guidance during this project. My thanks go to Gunnar Jacobi for his support on the CFD part of the project. He helped me a lot with the simulations, especially towards the final stages when time was limited. I would like to thank Oriol Colomes Gene for his involvement as a member of the committee.

I am especially grateful to my girlfriend, Eva, for her continuous support throughout both my bachelor's and master's studies. Finally, I would also like to thank my friends and family for their encouragement along the way. This work marks the conclusion of my studies and reflects both the challenges and the rewarding learning experiences encountered along the way. I am proud of the result and the progress that I've made throughout the process.

Joris Krämer
Rotterdam, May 2026

Abstract

Accurately predicting wave-induced forces plays an important role in ship design. Currently, pressure integration is the standard method for calculating wave-induced forces from panel methods. For Computational Fluid Dynamics (CFD) and experiments, it is not even possible to separate the wave-induced forces from the viscous forces. Pressure integration is limited by discretization, which can compromise the accuracy of the results. Wave pattern analysis offers an alternative by calculating wave-induced forces from the far-field wave elevation, thereby reducing the influence of discretization.

The transverse wave cut method (TWC) uses wave elevation measured along a single line perpendicular to the ship's path. Previous research has demonstrated that wave resistance can be determined using this method. Since only wave elevation data is necessary, wave resistance could even be calculated from experimental data.

No effort has been made yet to extend this method to calculate wave-induced side forces. This research investigates whether side forces can be accurately determined using the TWC method and evaluates its performance against conventional pressure integration in panel methods and CFD simulations.

The TWC method is derived from the conservation of momentum around the ship hull. The method applies a Fourier transform to the measured wave elevation to determine the free wave spectrum, which describes the wave field as a superposition of individual wave components. By reformulating the final expression, it is shown that the same spectral coefficients used to calculate the wave resistance can also be used to determine the wave-induced side force, without requiring any additional measurements or calculations.

The TWC method was compared with pressure integration results for a submerged spheroid using a panel method. Multiple test cases were considered, all of which showed good agreement between the two approaches. The TWC method was therefore successfully validated for calculating wave-induced side forces.

By plotting the free wave spectrum, the contributions of individual wave components at different propagation angles can be observed. As expected, the wave resistance was found to be dominated by the transverse wave components, while the side force was caused almost entirely by the diverging wave system.

In CFD simulations, the cell size strongly influences the quality of the simulated wave pattern. Coarser meshes introduce more numerical damping, causing the wave pattern to decay faster than physically expected. This was confirmed by evaluating the TWC method at multiple longitudinal locations, where the decay rate was extracted and compared across refinement levels. The numerical damping prevented accurate force predictions. However, the TWC method proved to be a useful diagnostic tool, providing a quantitative measure of wave decay and indicating the quality of the simulation.

Overall, the TWC method can accurately predict wave-induced side forces from a simulated wave field, showing good agreement with pressure integration for panel method results. In CFD simulations, its accuracy is limited by mesh resolution and numerical dissipation, but it can still be used as a diagnostic tool.

Contents

Nomenclature

Abbreviations

Abbreviation	Definition
CFD	Computational Fluid Dynamics
LCB	Lengthwise Center of Buoyancy
LWC	Longitudinal wave cut
PS, SB	Port side, Starboard
RANS	Reynolds-averaged Navier-Stokes
TWC	Transverse wave cut
VOF	Volume of Fluids
WASP	Wind Assisted Ship Propulsion

Symbols

Symbol	Definition	Unit
$A(\theta)$, $B(\theta)$	Free wave spectrum coefficients LWC	[-]
b	Width of wave cut	[]
c	Wave speed	[m/s]
c_g	Wave energy speed	[m/s]
c_1, c_2, c_3	Constants for asymptotic extension LWC	[-]
$C(u,x)$, $S(u,x)$	Cosine and sine component of Fourier transform	[-]
C_w	Non-dimensional wave resistance	[-]
C_y	Non-dimensional wave-induced side force	[-]
dx	Distance between wave cuts	[m]
$f(\theta)$, $g(\theta)$	Free wave spectrum coefficients as function of θ ($_e$ and $_o$ denote odd and even parts)	[-]
$\mathbf{f}$	Stress acting on the volume of a fluid	[N/m^3]
$F(u)$, $G(u)$	Free wave spectrum coefficients TWC as function of θ ($_e$ and $_o$ denote odd and even parts)	[-]
Fn	Froude number	[-]
g	Gravitational acceleration	[m/s^2]
h	Water depth	[m]
k	Wave number	[m^{-1}]
k_0	Fundamental wave number $\frac{g}{U^2}$	[m^{-1}]
L_{pp}	Length between perpendiculars	[m]
$\hat{n}$	Surface normal	[-]
p	Pressure	[Pa]
R_T	Total ship resistance	[N]
R_v	Viscous resistance	[N]
R_w	Wave resistance	[N]
Rn	Reynolds number	[-]
s	Longitudinal wave number	[m^{-1}]
S	Wetted surface	[m^2]
t	Time	[s]
$\mathbf{t}$	Stress acting on surface of a fluid	[Pa]
T	Wave period	[s]

Symbol	Definition	Unit
u	Transverse wave number	[m^{-1}]
$\mathbf{u}$	Velocity vector	[m/s]
U	Ship speed	[m/s]
x, y, z	Coordinates of ship fixed reference system	[m]
x_i	x-location of wave cut	[m]
X, Y	x and y force acting on the cylinder for the X-Y method	[N]
y^+	Non-dimensional wall distance	[-]
β	Drift angle	[°]
ϵ	Neumann's factor	[-]
ε	Phase of wave	[-]
ζ	Wave elevation	[m]
ζ'	Asymptotic extension of LWC	[m]
ζ_0	Averaged amplitude for the X-Y method	[m]
θ	Wave angle	[rad]
λ	Wave length	[m]
μ	Dynamic viscosity	[N s/m]
ν	Kinematic viscosity	[m^2/s]
ρ	Water density	[kg/m^3]
ϕ	Velocity potential	[m^2/s]
ϕ_x, ϕ_y, ϕ_z	Flow velocity components in x,y,z direction	[m/s]
$\hat{n}$	Surface normal	[-]
ω	Wave frequency	[rad/s]

1 Introduction

1.1. Background

In the design and engineering of a ship, the process is highly reliant on an accurate estimation of the hydrodynamic forces acting on the hull. For the early design phase, a good estimate is helpful for getting a general layout and specification for the ship. Also, for designing the hull, it is convenient to have a quick but accurate impression of how it will perform in real life. This makes it possible to properly adjust the hull to keep the ship's resistance as low as possible. Later in the design process, it can influence the technical specs of the vessel, such as the main engine and propeller. Contractual agreements have been made between the buyer and the shipyard. If the resistance prediction turns out wrong, the ship might not be able to sail at the speed agreed in the contract. Therefore, it is important to know the ship's resistance.

In 1870, W. Froude started using model tests to determine ship resistance. He found out that the resistance could be subdivided into skin frictional resistance and residuary resistance. With the residuary mainly consisting of wave resistance [20]. He also introduced the scaling laws (named after himself), which made it possible to convert model-size results to real-size results. Nowadays, model tests are still widely used for their accuracy. However, they are quite expensive.

Other methods in use include numerical and empirical methods. A well-known empirical method was developed by Holtrop and Mennen [11]. Especially in early ship design, these methods are useful because they are very simple, fast and inexpensive. It can be used when only the ship's main parameters are known. However, the result is relatively imprecise. These methods rely on conventional hull shapes; therefore, innovative designs will give inaccurate results.

Numerical methods are another way to predict the hydrodynamic forces acting on the ship. This can be subdivided into volume flow methods and boundary element methods. Volume methods like RANS take viscosity into account. They can be quite accurate, but are computationally expensive. Here, forces are calculated by integrating pressures and shear forces over the hull. Boundary element methods are based on potential flow (inviscid) and are much faster than volume methods, but they do not include friction. In the boundary element method, forces are calculated by integrating only the pressures, resulting in wave-induced forces. It turns out that the discretization has a large influence on the outcome. Therefore, this method can be imprecise.

Another way to calculate the forces acting on a ship is to use wave pattern analysis. The force is calculated from the far-field wave system, so this method should be less susceptible to the problems arising from pressure integration. It is based on momentum conservation analysis around the ship. This results in an expression for the wave resistance, which consists of a double integral of the local velocities in a plane behind or alongside the ship. For calculated wave fields, this integral can be used. For experiments, it can be difficult to obtain perturbation velocities below the surface. With the help of a Fourier transform, this can be rewritten such that only wave elevation data must be known for a line transverse or longitudinal to the hull. This makes it possible to calculate wave resistance from wave

elevation data from model tests or numerical methods.

1.2. Problem statement

In previous research on wave pattern analysis, the focus has been on calculating the force's resistance component. It is also of interest to determine side forces on a ship. Side forces can, for example, occur for ships with an asymmetrical hull (a sailboat under heel) or for ships sailing with wind-assisted propulsion (WASP). Wind-assisted propulsion is now being increasingly investigated as a way to reduce ship emissions. This makes the accurate prediction of side forces a relevant topic.

In a publication by Sharma (1964) [24], an expression for calculating the side force from wave pattern analysis can be found. No further research has been found on the testing of this expression.

1.3. Objective

The objective of this research is to use wave pattern analysis to determine the side force acting on a ship. To reach the goal, the following main research question will be answered:

Main:

- To what extent can side forces acting on a ship be accurately determined from a calculated wave field using the transverse wave cut method?

Sub-questions will be addressed to help answer the main question:

Sub:

1. How can a Fourier transform of the transverse wave cut be used to obtain the side force?
2. How does the side force obtained from the transverse wave cut method compare to that obtained from pressure integration under varying location, angle, speed, and grid size?
3. What insights can wave spectrum analysis provide for side forces?
4. To what extent can the transverse wave cut method be used in CFD simulations?

1.4. Approach and Scope

To answer the research question, a literature review on wave pattern analysis will be done. After this, a method for calculating the side force from a transverse wave cut will be developed. This method will be tested with results from two numerical simulations.

First, a panel method based on Neumann-Kelvin source panels written in the programming language Julia by Gabe Weymouth will be used. This is a linear solver using only source panels. The advantage of this method is that it is designed to be fast and flexible, so that different parameters of the wave cut method can be changed easily. This method will mostly be used for validation.

The next step will be to test the wave cut method in RANS CFD simulations. Results for the wave pattern will be obtained using the open-source software OpenFOAM. The results will show whether the method is valid for this application.

Two different test bodies will be considered. The flow field will be calculated using a panel method. Different drift angles and speeds can be used. Validation will be done using pressure integration and experimental results. The bodies used for testing are:

- **Spheroid**

  A non-surface-piercing spheroid has two key advantages: its simple shape and its fully submerged condition, which together reduce the factors influencing the flow.

- **Ecoliner**

  This ship has been designed to move under wind-assisted propulsion. It is a relevant test case, as side forces are often present under wind-assisted conditions.

The scope of this research is defined by the following limitations. This ensures that the research is concise and stays on topic. The limitations are:

- **Only transverse wave cut**

  Longitudinal wave cut will not be considered, because a transverse wave cut is considered more suitable for calculated wave fields.
- **Steady flow**

  Steady flow simulations will only be used. No time dependencies will be researched.
- **Infinite depth**

  Infinite depth will be assumed for all derivations.
- **Forward sailing**

  Reverse sailing or manoeuvring will not be taken into consideration. Only sailing under a drift angle will be investigated.
- **No incoming waves or channel effects**

  The ship is sailing in a uniform, homogeneous flow without waves and effects from walls.
- **No propeller effects**

  No propeller is simulated in the panel methods.
- **No wind effect**

  Effects due to wind will not be taken into consideration.

1.5. Thesis outline

The thesis will be structured as follows: First, the general theory of wave resistance and potential flow will be explained in chapter 2 as well as the momentum analysis of the wave pattern. After this, previous work on wave analysis methods will be explained in chapter 3. In chapter 4, the methodology is shown, and the method of the transverse wave cut is validated. Results for the testing of the transverse wave cut method on the wave field generated by a panel method or a CFD simulation will be given and discussed in chapter 5. Finally, chapter 6 presents the conclusion and recommendations for further research are given in chapter 7.

2

General theory

The theory behind wave pattern analysis will be explained in this chapter. This knowledge forms the foundation for the various techniques used to determine the forces acting on a ship. First, general comments and observations on wave resistance will be made, as the decomposition of forces is relevant to this subject. After this, an explanation of panel methods will be given. Linear wave theory will be discussed in the next section. VOF CFD methods will be explained after this. In the last section, a momentum-conservation analysis of a ship flow will be performed.

2.1. Wave resistance

When a ship is sailing at constant speed through the water, the following observations can be made. A region of turbulent flow can be seen along the ship and in the wake, and there is a wave pattern moving with the hull. These phenomena both cause drag on the hull and absorb energy. Total resistance of the hull is created by the shear and normal stresses on the hull's surface. This can be subdivided into wave and viscous resistance. Wave resistance is the subject of this literature review. It turns out that wave waking is rather insensitive to viscous effects [18]. With this in mind, the total resistance can be decomposed as:

$$R_T(Fn, Rn) \approx R_w(Fn) + R_v(Rn) \tag{2.1}$$

Wave resistance will be defined as the energy that flows from the ship to the wave pattern, divided by the ship's speed [17].

$$R_w = \frac{\text{energy transfer (ship} \rightarrow \text{waves)}}{\text{ship speed}} \tag{2.2}$$

The wave resistance coefficient is used to compare the wave resistance for different sizes and shapes. This is obtained by dividing the wave resistance by the product of the density, the square of the speed, and the wetted surface. This results in a non-dimensional coefficient:

$$C_w \equiv \frac{R_w}{\frac{1}{2}\rho U^2 S} \tag{2.3}$$

Wave resistance can be determined using numerical methods, empirical data, and experimental results. Most numerical methods, such as CFD and potential flow methods, use pressure integration to determine wave resistance.

2.2. Panel methods

Wave resistance can be determined using numerical or experimental methods. In this thesis, a Boundary Element Method (BEM) will be used to determine the wave pattern and flow around a ship's hull. These results can be used to obtain the wave-induced forces and validate the results of the wave cut method. BEM is a tool that uses potential flow. It is therefore important to have a theoretical understanding of potential flow. This section will explain potential flow. After this, BEM will be explained.

2.2.1. Potential theory

Potential flow theory is based on several assumptions. It assumes a fluid that is incompressible, inviscid, and irrotational. With these assumptions, the Navier-Stokes equation reduces to Laplace's equation.

$$\nabla^2 \phi = 0 \tag{2.4}$$

The velocity potential (scalar) is given by ϕ and describes the velocity field as follows:

$$\mathbf{u} = \nabla \phi \tag{2.5}$$

The pressure in the flow can be found using the Bernoulli equation:

$$\frac{1}{2}(\nabla \phi \cdot \nabla \phi) + \frac{p}{\rho} + gz = C \tag{2.6}$$

Introducing U as the ship's speed, calculating C at the water surface (z=0) gives the following equation for the entire flow field:

$$p = -\rho g z + \frac{1}{2}\rho(U^2 - \nabla \phi \cdot \nabla \phi) \tag{2.7}$$

Potential flow is a linear model. Therefore, superposition can be used to obtain a desired flow field. Singularities, such as sources, sinks, vortices, and dipoles, can be used to create a flow field. Combinations of these singularities can create a flow field that resembles a real flow around closed surfaces. This makes it possible to simulate inviscid flows analytically. For more complex shapes, numerical methods can be used.

Potential flow represents a flow at an infinite Reynolds number. A typical ship has a length-based Reynolds number of 10^9. This means that potential flow can provide a reasonable representation of the flow around a ship's hull. For wave patterns, viscous effects are usually very low [18]. Especially in the far-field propagation of waves, the viscous effects are negligible. For this inviscid flow model, the wave resistance is often the largest resistance component. This is because most of the energy leaves the system by traveling waves moving away from the ship.

2.2.2. BEM

Boundary Element Methods (BEM), or panel methods, use potential flow to calculate flow numerically. A discretization of the hull is created, and source panels are placed at each grid point. Each panel, like a point source, induces a velocity and potential field. Using a panel source instead of a point source has the advantage that the panel source does not tend to infinity near the center. The panel source tends to a constant velocity.

Only the panel source strengths are unknown. The use of a Green's function that includes the free-surface boundary condition will give a solution such that the boundary conditions will be satisfied. For a flow around a body, it cannot pass through the body. Therefore, the velocity normal to the surface should always be zero. This is the kinematic boundary condition.

$$\mathbf{v} \cdot \hat{n} = \frac{\partial \phi}{\partial n} = 0 \tag{2.8}$$

Another important boundary condition is the dynamic free surface condition. This ensures that the pressure at the surface equals atmospheric pressure. This can be done by filling in Equation 2.6 far upstream at $z = \zeta$ and $\nabla\phi = U$. With this, the wave elevation can be calculated if the potential is known on the free surface. This gives the following condition:

$$\zeta = \frac{1}{2g}(U^2 - \nabla\phi \cdot \nabla\phi) \tag{2.9}$$

After linearizing, this results in:

$$\zeta = -\frac{U}{g}\phi_x \tag{2.10}$$

The kinematic boundary condition ensures that the flow near the free surface remains along the surface.

$$\phi_x \frac{\partial\zeta}{\partial x} + \phi_y \frac{\partial\zeta}{\partial y} - \phi_z = 0 \text{ at } z = \zeta \tag{2.11}$$

Other relations are the bottom boundary condition (no flow through the sea floor) and the radiation condition. The radiation condition requires that all generated waves remain behind the ship, ensuring that the ship advances into calm, undisturbed water.

It is possible to add viscosity effects with empirical formulas to estimate the full resistance of a ship using, for example, the ITTC 1957 correlation line [18]. This gives the frictional resistance as:

$$C_F = \frac{0.75}{(log_{10}Re - 2)^2} \tag{2.12}$$

BEM uses surface discretization and therefore the resolution scales with N^2. This makes it less computationally expensive than CFD methods, for example, RANS calculations. These methods use volume discretization and scale with N^3. Since the Reynolds number for ships is typically very high, BEM provides an accurate description of the flow field, making it a useful and fast tool in ship hydrodynamics.

2.2.3. Pressure integration

The most common method for determining the forces acting on the body using CFD is to integrate the pressure over the hull. This gives the forces in x, y, and z directions. The pressures will be calculated using Bernoulli's equation as stated previously in Equation 2.7. For the wave resistance, the x-direction is needed. The formula for each direction is:

$$F_i = -\iint_S p \cdot \hat{n}\, dS \tag{2.13}$$

It turns out that pressure integration is not very accurate when a large bow wave exists. Similarly, negative wave resistance can occur when the stern wave is overestimated. This can occur for canoe-like stern hulls sailing at low speeds. [1]

2.3. Linear wave theory

A single mathematical solution for wave patterns does not exist in most cases. To understand complex wave systems, it is necessary to understand a single wave. These can be described as a sine or cosine function. This model assumes that the flow is inviscid, irrotational, homogeneous, and incompressible. This is justified, as the viscous effects on the wave propagation are entirely negligible for ship scales. [18]. A linear representation of the wave can be given as:

$$\zeta = \zeta_a \cos(sx + uy - \omega t + \varepsilon) \tag{2.14}$$

Here, $s = k\cos(\theta)$ and $u = k\sin(\theta)$, with k being the wave number. Since the flow is both irrotational and incompressible, the velocity potential should satisfy the Laplace equation $\nabla^2\phi = 0$. Together with the dynamic boundary condition at the surface and the boundary condition at the bottom, the velocity potential can be determined. The dynamic boundary condition at the surface uses the linearized Bernoulli equation. Quadratic velocity terms are omitted, which can be done for waves with minor steepness. This results in the following expression for the velocity potential:

$$\phi = \frac{\zeta_a g}{\omega}\frac{\cosh(k(h+z))}{\cosh(kh)}\sin(sx + uy - \omega t + \varepsilon) \tag{2.15}$$

For deep water $\frac{\cosh(k(h+z))}{\cosh(kh)}$ reduces to e^{kz}. This approximation holds when $kh \gg 1$.

$$\phi = \frac{\zeta_a g}{\omega}e^{kz}\sin(sx + uy - \omega t + \varepsilon) \tag{2.16}$$

With these potentials, the velocity at every point in the flow can be calculated by the derivatives of the potential in x, y, and z directions.

The relation between the frequency (ω) and the wave number (k) can be found from the kinematic boundary condition near the free surface. After linearizing the condition and filling in the wave potential, the following expression is obtained.

$$\omega^2 = kg\tanh(kh) \tag{2.17}$$

Using Bernoulli's equation (2.6), the pressures in the flow can be determined on and below the surface. Other important relations for wave number, frequency, phase speed, and group speed are:

$$k = \frac{2\pi}{\lambda} \qquad \omega = \frac{2\pi}{T} \qquad c = \sqrt{\frac{g}{k}\tanh(kh)} \qquad c_g = \frac{1}{2}c\left(1 + \frac{2kh}{\sinh(2kh)}\right) \tag{2.18}$$

Linear wave theory is based on the assumption that the waves have a small amplitude relative to the wavelength. Under these conditions, the equations can be linearized, and the superposition principle holds. This makes it possible to represent irregular wave fields as a sum of regular waves. With this, the potential of the entire field can be determined, which makes it possible to find the local velocities and pressures. This decomposition into regular components forms the basis of wave pattern analysis.

Limitations of Linear Wave Theory Near the Ship Hull

Near the ship, non-linear effects are often present. The geometry of the hull influences the flow, locally amplifying waves and increasing their steepness, violating the small-steepness assumption. In more extreme cases, it can lead to wave breaking and spray. Both the kinematic and dynamic boundary conditions were linearized and applied at the mean water surface $z = 0$. For steep waves, this assumption also breaks.

Finally, near the bilge and stern, the flow can separate from the hull, generating vorticity and directly violating the irrotational flow assumption that underlies the velocity potential formulation. Together, these effects mean that the quadratic terms dropped in the linearization of the governing equations are no longer small near the ship, and higher-order methods are required to accurately capture near-field flow. Superposition of linear waves to capture the wave field near the hull is therefore not possible.

2.4. CFD methods

In this study, CFD methods will also be used to calculate the wave field. Wave pattern analysis can be applied to the generated wave pattern. Unlike potential flow methods, CFD solves the Navier–Stokes equations, so it accounts for viscous effects. This makes it possible to produce more physically realistic wave patterns and force predictions. However, this increased fidelity comes at the cost of greater complexity and calculation time. Some basic background on CFD methods for ship hydrodynamics will be presented in this section.

2.4.1. Navier-Stokes equations

CFD methods solve the Navier-Stokes equations. The Navier-Stokes equations consist of general conservation laws on mass and momentum, given at a single point. For ship applications, the flow is assumed to be incompressible, which is a reasonable assumption for liquid substances. Mass conservation is given as:

$$\frac{\partial \rho}{\partial t} + \nabla \cdot (\rho u) = 0 \tag{2.19}$$

The momentum equation is given as:

$$\rho(\frac{d\mathbf{u}}{dt} + \mathbf{u} \cdot \nabla \mathbf{u}) = -\nabla p + \mu \nabla^2 \mathbf{u} + \mathbf{f} \tag{2.20}$$

This is a vector equation in x, y and z direction. The vectors are given in bold. $\rho(\frac{d\mathbf{u}}{dt} + \mathbf{u} \cdot \nabla \mathbf{u})$ is the inertial term, consisting of a time-dependent term and a non-linear term. $\mathbf{u} \cdot \nabla \mathbf{u})$ is the only non-linear term in the equation. This term physically relates to the convection of velocity gradients through the flow due to the velocity. In this term, a small perturbation in the velocity can cause a small perturbation in the velocity gradient, which affects the other terms in the equation, and a change in time can be found. These changes can cause more change in perturbation velocity, and the cycle continues. This can result in chaos, i.e., turbulence. This term makes the equation difficult to solve, as it is infinitely sensitive to initial or boundary conditions. For steady flows, which will be the case for this study, the time-dependent term will vanish, as the wave pattern moves steadily with the ship.

On the right-hand side, the equation consists of a pressure term ($-\nabla p$), a viscous term ($\mu \nabla^2 \mathbf{u}$), and the force term ($\mathbf{f}$). The force term can be any body force acting on the flow. For ship applications, this is the gravity force.

2.4.2. Simulation methods

In order to capture all turbulence effects, the method requires the use of a mesh and time step that are able to resolve the smallest dissipative length scale, the Kolmogorov scale. This approach is called Direct Numerical Simulation (DNS), and it solves the equations exactly without any turbulence models. It requires a very fine mesh and a small time step, which is not feasible for ship applications. Therefore, different models are developed to model turbulent effects.

Large-Eddy Simulation (LES) is a mathematical model for turbulence. LES reduces the computational costs by filtering out the smallest length scales. The large Eddies, containing more energy, are resolved directly, while the smaller Eddies are modeled. This significantly reduces costs compared with DNS. For simulating at ship scale, this is often still too expensive to compute.

RANS

Reynolds-Averaged Navier-Stokes (RANS) is another mathematical model with lower fidelity than DNS and LES. The flow motions are being decomposed into mean components $\overline{\mathbf{u}}$ and fluctuating $\mathbf{u}'$ component, which is called the Reynolds decomposition and is given as:

$$\mathbf{u} = \overline{\mathbf{u}} + \mathbf{u}' \tag{2.21}$$

Substituting this in the momentum equation and averaging over time gives:

$$\rho(\frac{d\overline{\mathbf{u}}}{dt} + \overline{\mathbf{u}} \cdot \nabla \overline{\mathbf{u}}) = -\nabla p + \mu \nabla^2 \overline{\mathbf{u}} + \mathbf{f} - \nabla(\rho \mathbf{u}' \mathbf{u}') \tag{2.22}$$

This introduces the Reynolds stress tensor, given as $\nabla(\rho \mathbf{u}' \mathbf{u}')$ on the right side of the equation. This term introduces six more terms, resulting in more unknowns than equations. To close the system, a turbulence model is required.

2.4.3. Turbulence model

The turbulence model is introduced to close the system of equations. Multiple models are available, but no universal model has been developed. The best model varies by application. Most models are based on the Boussinesq hypotheses, which introduce a turbulent (or eddy) viscosity to represent the influence of turbulent motion on the mean flow. A complete overview of different turbulence models can be found in Wilcox (2006) [28]. For ships, the k-ω turbulence model is by far the most applied model. This is a two-equation model; one equation solves for the turbulence kinetic energy (k), the other for its specific dissipation rate (ω). It has been shown that these models give accurate predictions for ship hydrodynamics. [12]

2.4.4. Generic transport equation

The RANS equations and the turbulence model equations (k-ω) can be written into a generic differential equation [18]:

$$\underbrace{\rho\frac{\partial\phi}{\partial t}}_{\textit{Transient}} + \underbrace{\rho\nabla\cdot(\mathbf{u}\phi)}_{\textit{Convection}} = \underbrace{\nabla\cdot(\Gamma\nabla\phi)}_{\textit{Diffusion}} + \underbrace{S}_{\textit{Source}} \tag{2.23}$$

Here, ϕ is the general dependent variable, such as $\mathbf{u}$, k or ω. The physical interpretation of each term is given below. The transient term is relevant for unsteady problems. When computing the calm water resistance of a ship, the flow may be considered steady. The convection term represents the transport of the variable by the velocity of the fluid. The first term on the right side represents the rate of increase due to diffusion, which is related to viscosity and damping. The source term accounts for anything that creates or destroys the quantity.

2.4.5. Numerical Schemes

Numerical schemes in CFD are used to discretize the governing equations in space and time. The choice of the method can strongly affect accuracy and stability. Different numerical schemes can be used for different aspects of the simulation.

All terms in Equation 2.23 need a numerical discretization scheme. The source term has no derivatives, so it does not need a discretization scheme. For steady flow, the transient term is assumed to be zero for a ship simulated in still water. Diffusion terms are naturally stabilizing. In most CFD codes, these terms are discretized using a second-order (central-difference) scheme. Spatial accuracy is therefore mostly determined by the discretization of convective terms.

The convective term is the only non-linear term in the equation. Therefore, it can cause oscillations and instability. This makes it highly sensitive to the choice of discretization. Different order schemes can be chosen. Lower-order schemes are very stable but introduce large numerical diffusion, while higher-order schemes provide less numerical diffusion but can be unstable. The majority today are second order with an upwind bias [12]. Upwind bias means that more weight is given to values in the upstream direction. Every CFD needs some numerical dissipation in order to obtain a stable result.

2.4.6. Free surface

A ship is always sailing on the interface between air and water. Therefore, special treatment is required to simulate this interface. The free surface (interface) can be modeled using a Volume of Fluid (VOF) method. A scalar (α) defines how much of each cell is water or air. If $\alpha = 0$, the cell is filled with air, and if $\alpha = 1$, the cell is filled with water. At the interface, the cell is partially filled with water, and the scalar can be used to find the average density and viscosity in the cell.

2.4.7. Turbulence near the wall

Near the wall, flow variables have large normal gradients. Turbulent fluctuations are suppressed by viscous effects and dominate the momentum transfer. Proper modeling is required for this region. Two methods are available:

- **Near wall turbulence model:** Using near-wall turbulence models that can resolve the flow down to the wall

- **Wall functions:** Use semi-empirical formulae to model the flow that is closest to the wall.

The non-dimensional wall distance can be introduced to further analyze the methods as:

$$y^+ = \frac{y * u_t}{\nu} \tag{2.24}$$

Here, u_t is the friction velocity, ν is the kinematic viscosity, and y is the dimensional distance from the wall. For the near-wall turbulence model, the first cell height should be at $y^+ < 1$. Only then can the simulation fully resolve the flow in the wall region. It leads to high aspect ratios, which can cause numerical instability.

A reduction in cell count is observed when the flow is modeled using wall functions. For this approach, the y^+ value is usually between $30 \leq y^+ \leq 100$. This reduces the extreme refinements near the wall at the cost of being less accurate, as wall functions are an estimate of actual flow in the boundary layer. If possible, it is better to avoid wall functions; they should be handled with care.

2.4.8. Meshing

Meshing is an important part of any CFD simulation. In general, a fine mesh can more accurately simulate the flow. Large cells are more prone to wave damping. Since it is not feasible to use a very fine mesh everywhere in the domain due to excessive computational time, it is important to refine the mesh in important regions. This can be done by defining refinement regions, which provide refinement where it is necessary but use a coarser mesh elsewhere. Often, refinement regions are generated near the bow and stern of the ship, as the flow is usually more complex in these locations (large pressure gradients). For free-surface simulations, it is advised to make a refinement region to limit the numerical errors in the free surface. This can require around 50 cells per wavelength. This ensures that wave damping is minimized, and the interface stays sharp [18].

Near the surface of the hull, the mesh must be aligned parallel to the hull to resolve the large wall normal gradients. The mesh here consists of several layers of hexahedral cells that grow in thickness away from the hull. The height of the first cell is defined by the y^+ value of the turbulence model.

At the edges of the domain, the mesh can be very coarse, which serves two purposes. Firstly, the flow near the boundary is undisturbed, so no fine mesh is needed, which reduces the computational time. Secondly, the coarser cells introduce more numerical diffusion, which absorbs the waves before they reach the boundary and reflect back into the domain.

Meshing affects numerical dissipation in CFD through three main factors: resolution, alignment, and quality. A coarse mesh cannot properly resolve flow features such as waves or turbulence, leading to artificial damping, whereas a finer mesh reduces this effect by better capturing the solution. If the mesh is not aligned with the flow direction, the solution must be reconstructed across multiple directions, introducing diffusion. In addition, poor mesh quality, such as skewness, non-orthogonality, or abrupt changes in cell size, introduces additional errors that often behave like artificial diffusion. In general, coarse, misaligned, or low-quality meshes increase numerical dissipation, whereas fine and well-structured meshes minimize it.

2.4.9. Postprocessing

After the simulation is complete, postprocessing can be used to extract relevant physical quantities from the CFD results, including forces, flow properties, and pressure distributions. All forces and moments can be computed by integrating the pressure and viscous stresses over the hull surface. Flow properties can be used to gain information about the wave pattern and other flow components. These results are often visualized using contour plots or vector fields and can be compared with experimental or reference data.

2.4.10. Wave pattern

For this study, the primary focus is on the wave pattern generated by the ship, as it is the subject of analysis. Accurate prediction of the free surface is therefore important. This requires a free-surface

simulation method. Special care must be taken to minimize numerical damping, as excessive diffusion can lead to an underprediction of wave amplitudes.

The choice of mesh and discretization plays an important role in this respect. Hexahedral cells are preferred, as they introduce less numerical damping than more irregular cell types. In addition, sufficient spatial resolution is required. It is recommended to use about 50 cells per wavelength. [18] Mesh refinement within the Kelvin wake is also recommended to better capture wave patterns.

Turbulence modeling is of secondary importance for wave prediction, since surface waves are generally only weakly affected by turbulence. Nevertheless, within a RANS framework, it is known that while the wave profile along the hull is typically predicted with reasonable accuracy, waves further away tend to be overly damped due to numerical and modeling effects [18].

2.5. Momentum conservation

To find the resulting wave forces of a ship via wave pattern analysis, information about the wave pattern must be known. This can be obtained either by experimental tests or numerical results. Wave cut methods are based on momentum conservation in a control volume box around the hull. Conservation will be derived for a transverse and longitudinal wave cut. For this analysis, a right-handed ship-fixed coordinate system will be defined with x in the flow direction and z in the upward direction. The flow is assumed to be steady, inviscid, irrotational, and incompressible. The ship will be traveling at constant speed U. Total momentum balance for a control volume is given by:

$$\frac{d}{dt}\iiint_{CV} \rho \mathbf{u}\, dV + \oiint_{CS} \rho \mathbf{u}\mathbf{u} \cdot n\, dS = \iiint_{CV} \mathbf{f}\, dV + \oiint_{CS} \mathbf{t}\, dS \tag{2.25}$$

Since it is a steady flow, $\frac{d}{dt} = 0$. The left side of the equation leaves only the momentum flux term. The right side consists of the forces acting on the fluid. Since there is no gravitational force in the x or y direction, the first term is zero. This leaves:

$$\left[\oiint_{CS} \rho \mathbf{u}\mathbf{u} \cdot \hat{n}\, dS = \oiint_{CS} \mathbf{t}\, dS\right] \cdot \hat{x} \tag{2.26}$$

2.5.1. Transverse wave cut

In Figure 2.1, the ship-fixed control volume can be seen. Due to the Kelvin angle, the wave pattern spreads out at a constant angle relative to the ship. The control volume should be chosen so that the waves generated by the ship only exit the system on the face behind the ship. This way, only the front and back faces need to be considered in the momentum balance.

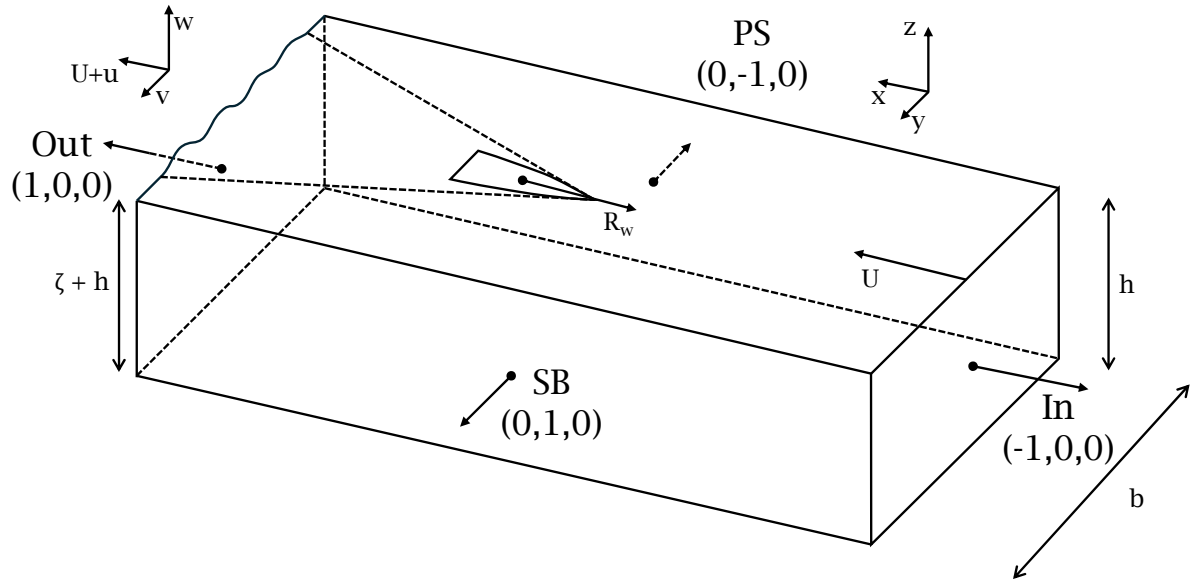

Figure 2.1: Control volume for momentum conservation

Since there is no flow through the top, sides, and bottom, only the in- and out-planes need to be considered for continuity of flow. Conservation of mass gives the following equation:

$$Ubh = \int_{-b/2}^{b/2} \int_{-h}^{\zeta_{out}} (U + \phi_x)\, dz\, dy \tag{2.27}$$

The momentum flux (left part of Equation 2.26) through the in-plane is given by:

$$M_{in} = \left[\int_{-b/2}^{b/2} \int_{-h}^{0} \rho \begin{bmatrix} U \\ 0 \\ 0 \end{bmatrix} \begin{bmatrix} U \\ 0 \\ 0 \end{bmatrix} \cdot \begin{bmatrix} -1 \\ 0 \\ 0 \end{bmatrix} \, dz\, dy \right] \cdot \begin{bmatrix} 1 \\ 0 \\ 0 \end{bmatrix} = -\rho U^2 \cdot b \cdot h \tag{2.28}$$

Substituting for $U \cdot b \cdot h$ from Equation 2.27 gives:

$$M_{in} = -\rho \int_{-b/2}^{b/2} \int_{-h}^{\zeta_{out}} U(U + \phi_x)\, dz\, dy \tag{2.29}$$

The momentum flux through the out-plane is given by:

$$M_{out} = \left[\int_{-b/2}^{b/2} \int_{-h}^{\zeta_{out}} \rho \begin{bmatrix} U + \phi_x \\ v \\ w \end{bmatrix} \begin{bmatrix} U + \phi_x \\ v \\ w \end{bmatrix} \cdot \begin{bmatrix} 1 \\ 0 \\ 0 \end{bmatrix} \, dz\, dy \right] \cdot \begin{bmatrix} 1 \\ 0 \\ 0 \end{bmatrix} = \rho \int_{-b/2}^{b/2} \int_{-h}^{\zeta_{out}} (U + \phi_x)^2\, dz\, dy \tag{2.30}$$

For the side, top, and bottom plane, this part of the equation results in zero as no flow passes through these surfaces, so $\mathbf{uu} \cdot \hat{n} = 0$. Adding each surface (in and out) together gives a total for the left side of Equation 2.26:

$$M_{in} + M_{out} = \rho \int_{-b/2}^{b/2} \int_{-h}^{\zeta_{out}} \phi_x (U + \phi_x)\, dz\, dy \tag{2.31}$$

The right part of Equation 2.26 consists of the forces acting on the fluid. Again, the side, top, and bottom faces are zero because they do not contribute to a momentum in the x direction. Therefore, the right-hand side consists of the integrated pressure forces on the in- and out-plane and the resistance force of

the hull. Bernoulli's equation is used to calculate pressures in the flow. The use of the Bernoulli equation in the following form is only valid for a flow that is steady, inviscid, irrotational, and incompressible. The assumption is justified, as the edges of the control volume faces are placed far from the hull.

$$\frac{p}{\rho} + \frac{1}{2}(\nabla\phi \cdot \nabla\phi) + gz = \text{constant} \tag{2.32}$$

At the undisturbed surface, $p_{atm} = 0$, $z = 0$ and $\nabla\phi \cdot \nabla\phi = U^2$. This gives the pressures for the in- and out-plane as:

$$p_{in} = -\rho g z \tag{2.33}$$

$$p_{out} = -\rho(gz + \frac{1}{2}(2U\phi_x + \phi_x^2 + \phi_y^2 + \phi_z^2)) \tag{2.34}$$

Resulting in:

$$F_{in} = \int_{-b/2}^{b/2}\int_{-h}^{0} p_{in} \cdot \hat{n}\, dz\, dy = -\rho g \int_{-b/2}^{b/2}\int_{-h}^{0} z\, dz\, dy = \frac{1}{2}\rho g \int_{-b/2}^{b/2} h^2\, dy = \frac{1}{2}\rho g b h^2 \tag{2.35}$$

$$\begin{aligned} F_{out} &= \int_{-b/2}^{b/2}\int_{-h}^{\zeta_{out}} p_{out} \cdot \hat{n}\, dz\, dy = \rho \int_{-b/2}^{b/2}\int_{-h}^{\zeta_{out}} [gz + \frac{1}{2}(2U\phi_x + \phi_x^2 + \phi_y^2 + \phi_z^2)] dz\, dy \\ &= \frac{1}{2}\rho g \int_{-b/2}^{b/2} (\zeta_{out}^2 - h^2)\, dy + \frac{1}{2}\rho \int_{-b/2}^{b/2}\int_{-h}^{\zeta_{out}} [2U\phi_x + \phi_x^2 + \phi_y^2 + \phi_z^2]\, dz\, dy \\ &= \frac{1}{2}\rho g \int_{-b/2}^{b/2} \zeta_{out}^2\, dy - \frac{1}{2}\rho g b h^2 + \frac{1}{2}\rho \int_{-b/2}^{b/2}\int_{-h}^{\zeta_{out}} [2U\phi_x + \phi_x^2 + \phi_y^2 + \phi_z^2]\, dz\, dy \end{aligned} \tag{2.36}$$

The last contribution is the ship's resistance (R_w) exerted on the flow. It can be entered directly into the equation, as it is already modeled as a force. Now that each contribution has been calculated, the total momentum equation can be filled in as:

$$M_{in} + M_{out} = F_{in} + F_{out} - R_w \tag{2.37}$$

This gives:

$$\begin{aligned} \rho \int_{-b/2}^{b/2}\int_{-h}^{\zeta_{out}} \phi_x(U + \phi_x)\, dz\, dy = \frac{1}{2}\rho g b h^2 + \frac{1}{2}\rho g \int_{-b/2}^{b/2} \zeta_{out}^2\, dy - \frac{1}{2}\rho g b h^2 \\ + \frac{1}{2}\rho \int_{-b/2}^{b/2}\int_{-h}^{\zeta_{out}} [2U\phi_x + \phi_x^2 + \phi_y^2 + \phi_z^2]\, dz\, dy - R_w \end{aligned} \tag{2.38}$$

Rewritten and simplified, this results in:

$$\boxed{R_w = \frac{1}{2}\rho g \int_{-b/2}^{b/2} \zeta_{out}^2\, dy + \frac{1}{2}\rho \int_{-b/2}^{b/2}\int_{-h}^{\zeta_{out}} (-\phi_x^2 + \phi_y^2 + \phi_z^2)\, dz\, dy} \tag{2.39}$$

This derivation is equal to the one presented in the book Ship Resistance and Propulsion by Molland, Turnock, and Hudson [20], and the result is equal to the one Eggers presented [4].

A similar concept in aerodynamics is known as the Treffz plane. It uses a similar momentum-conservation approach in a transverse plane in the far field downstream of a lifting body. The main difference is that the body is fully submerged in the fluid (air), thus no wave patterns exist. A derivation of the Treffz plane can be found in Katz (1991) [15].

The most straightforward way to evaluate the wave resistance from a flow field is to directly evaluate Equation 2.39. For this, local velocities and wave elevations must be computed using the panel method. The velocities and elevations should be calculated at a vertical plane behind the ship. The plane should be wide enough to capture all the waves and be sufficiently far away from the hull so that non-linear effects are minimized. Not much research has been done on this. Kömpe (2015) [17] used the direct integral. Contrary to expectations, direct integration was not consistent across different x-locations of the wave cut. Taking the average of multiple wave cuts was sufficient to solve this. This method technically cannot be regarded as a wave cut method, as the required input includes not only wave elevation data but also perturbation velocity data beneath the free surface.

2.5.2. Longitudinal wave cut

Similarly to a transverse wave cut, a longitudinal wave cut formula can also be derived. In this case, the control volume block will be chosen so that all momentum flux only transfers through the sides of the box. This results in infinitely long side boundaries. A full derivation of this can be found in Appendix A. This results in the following formula:

$$R_w = 2\rho \int_{-\infty}^{\infty} \int_{-h}^{\zeta} \phi_x \phi_y \, dz \, dx \tag{2.40}$$

In the paper by Eggers [4], this result was also shown. As can be seen in Equation 2.40, the side boundaries must be very long to ensure that all the momentum is contained within this barrier. In practice, this is difficult to realize.

2.5.3. Transverse wave cut side force

In section 2.5.1, it has been shown that the drag force can be calculated by using a transverse wave cut using momentum conservation in the x-direction. This project aims to determine the side force from the wave pattern. The first step is to perform the momentum conservation analysis in the y-direction for a transverse wave cut. The aim is to obtain the side force on a ship. The derivation again starts with the general (reduced) moment equation, now in the y-direction:

$$\left[\oiint_{CS} \rho \mathbf{u}\mathbf{u} \cdot \hat{n} \, dS = \oiint_{CS} \mathbf{t} \, dS \right] \cdot \hat{y} \tag{2.41}$$

First, the left side will be solved. The sides, top, bottom, and in-plane all result in 0 as $\mathbf{u}\mathbf{u} \cdot \hat{n} = 0$. For the out-plane, the following result is found:

$$M_{out} = \left[\int_{-b/2}^{b/2} \int_{-h}^{\zeta_{out}} \rho \begin{bmatrix} U + \phi_x \\ \phi_y \\ \phi_z \end{bmatrix} \begin{bmatrix} U + \phi_x \\ \phi_y \\ \phi_z \end{bmatrix} \cdot \begin{bmatrix} 1 \\ 0 \\ 0 \end{bmatrix} \, dz \, dy \right] \cdot \begin{bmatrix} 0 \\ 1 \\ 0 \end{bmatrix} = \rho \int_{-b/2}^{b/2} \int_{-h}^{\zeta_{out}} (U + \phi_x)\phi_y \, dz \, dy \tag{2.42}$$

For the right side of the equation, the top, bottom, in, and out planes are zero, as the pressure force acts in the x-direction. The SB and PS planes are far enough away to have undisturbed flow. Therefore, the pressures are equal but in opposite directions. This results in a net zero force from the sides. The force exerted in the y-direction by the hull is the only component for the right-hand side from Equation 2.41.

$$\oiint_{CS} \mathbf{t} \, dS = F_y \tag{2.43}$$

In total, this results in:

$$\boxed{F_y = \rho \int_{-b/2}^{b/2} \int_{-h}^{\zeta} (U + \phi_x)\phi_y \, dz \, dy} \tag{2.44}$$

Via this simple equation, it is possible to determine the side force on a ship's hull when velocities behind the ship are known. This result corresponds to the result given by Sharma (1964) [24]. However, no derivation was given. This was the only work found that considered calculating the side force from a transverse wave cut.

3

Previous work

In the previous chapter, the basic theory necessary for wave pattern analysis was discussed. In this chapter, further explanation of the different approaches of wave pattern analysis is presented.

3.1. Havelock

Havelock was among the first to investigate wave resistance by analyzing the wave pattern. In his paper from 1927 [8], he shows how to obtain wave resistance by examining the flow of energy in the wave motion. Later in 1934, the method was extended to three-dimensional problems [7]. Again, a steady potential flow is assumed. He proposes to describe the wave elevation in the far-field as:

$$\zeta = \int_{-\frac{\pi}{2}}^{\frac{\pi}{2}} f(\theta) \sin\left(k_0 \sec^2\theta \, \left(x\cos\theta + y\sin\theta - ct\cos\theta\right)\right) d\theta \tag{3.1}$$

He assumes that the pattern is symmetric about the x-axis and extends infinitely deep. This results in the following formula with $x' = x - ct$:

$$\zeta = 2\int_{0}^{\frac{\pi}{2}} f(\theta) \sin\left(k_0 x' \sec\theta\right) \cos\left(k_0 y \sin\theta \sec^2\theta\right) d\theta \tag{3.2}$$

And:

$$\phi = 2c\int_{0}^{\frac{\pi}{2}} f(\theta)\, e^{k_0 z \sec^2\theta} \cos\left(k_0 x' \sec\theta\right) \cos\left(k_0 y \sin\theta \sec^2\theta\right) \cos\theta \, d\theta \tag{3.3}$$

With these formulas, he calculates the rate of energy flow at a fixed vertical plate at $x =$ constant. The total flow of energy across this plane is:

$$\frac{1}{2}\rho c \int_{-\infty}^{0} dz \int_{-\infty}^{\infty} \left[\left(\frac{\partial\phi}{\partial x}\right)^2 + \left(\frac{\partial\phi}{\partial y}\right)^2 + \left(\frac{\partial\phi}{\partial z}\right)^2\right] dy + \frac{1}{2}\rho g c \int_{-\infty}^{\infty} \zeta^2 \, dy \tag{3.4}$$

This equation is already very similar to Equation 2.39 that has been derived in chapter 2 for the transversal wave cut. The only difference is that this formula has been multiplied by a factor c, which represents the ship speed. This is because it is the rate of energy and not momentum.

The variable part of the fluid is the pressure. The work done across the plane is:

$$\rho c \int_{-\infty}^{0} dz \int_{-\infty}^{\infty} \left(\frac{\partial\phi}{\partial x}\right)^2 dy \tag{3.5}$$

Filling in these equations with the previous description of the wave height and potential gives the following result for the flow of energy:

$$\pi\rho c^3 \int_0^{\frac{\pi}{2}} [f(\theta)]^2 \left[(3-\sin^2\theta)\sin^2\left(k_0 x' \sec\theta\right) + (1+\sin^2\theta)\cos^2\left(k_0 x' \sec\theta\right)\right] \frac{\cos^3\theta \; d\theta}{1+\sin^2\theta} \tag{3.6}$$

And for the rate of work:

$$2\pi\rho c^3 \int_0^{\frac{\pi}{2}} [f(\theta)]^2 \sin^2\left(k_0 x' \sec\theta\right) \frac{\cos^5\theta \; d\theta}{1+\sin^2\theta} \tag{3.7}$$

These results are independent of the plane's position and time. Subtracting the two results gives the rate at which energy is being propagated. Two vertical planes are considered. One plane is located far upstream, and the other is located behind the ship. The difference must be equal to the flow of energy across the vertical planes, which is equal to $R_w c$. Combining these results in:

$$R_w = \pi\rho c^2 \int_0^{\frac{\pi}{2}} [f(\theta)]^2 \cos^3\theta \; d\theta \tag{3.8}$$

This formula can also be rewritten in terms of sine and cosine components [18]:

$$R_w = \frac{1}{2}\pi\rho c^2 \int_{-\frac{\pi}{2}}^{\frac{\pi}{2}} [A(\theta)^2 + B(\theta)^2] \cos^3\theta \; d\theta \tag{3.9}$$

By integrating over the wave spectrum, the wave resistance can be obtained. This expression shows that the wave resistance depends quadratically on amplitude and that the phase does not influence the resistance. The factor $\cos^3\theta$ shows that transversal (small θ) waves have a much larger influence on the wave resistance than diverging waves (large θ).

In the same paper from 1934 [7], Havelock derives the expression for finite depth. This results in the following equation:

$$R_w = \frac{1}{2}\pi\rho c^2 \int_{-\frac{\pi}{2}}^{\frac{\pi}{2}} [f(\theta)]^2 \left(\frac{\cosh kh}{\sinh kh} - \frac{kh}{\sinh^2 kh}\right) \cos^3\theta \; d\theta \tag{3.10}$$

In this paper, Havelock presents a method to describe the flow and wave pattern. From this, he shows how to obtain wave resistance. He doesn't show how to obtain the wave constants $f(\theta)$. However, it can still give physical insight into the wave resistance.

3.2. Wave cut methods

The problem with using the momentum derivation results from chapter 2 is that the velocities of the entire plane must be known. With an experimental setup, this is very difficult to measure. It is often only feasible to obtain wave elevation data from measurements. However, with linear wave theory, it is still possible to obtain these velocities using a Fourier transformation. This section explains the working of wave cut methods.

The entire wave field can be composed of a sum of singular waves, called the free wave spectrum. The mathematical representation and corresponding assumptions of these waves can be found in section 2.3. Havelock described a formula for determining the wave resistance from this decomposition, but did not show how to obtain the parameters of the free wave spectrum. A transverse or longitudinal wave cut method can be used to determine the free wave spectrum. Each method is based on its momentum derivations previously described (as given in chapter 2).

Eggers proposed a method in 1962 [4] to determine the wave resistance from a wave cut. This paper was later translated for the International Seminar on Theoretical Wave Resistance [3]. It can also

be found in state-of-the-art papers from Eggers, Sharma, and Ward (1967) [5] and Eggers (1975) [2]. The following derivations mostly follow Eggers, Sharma, and Ward (1967) [5] and use the same axis orientation and notation.

3.2.1. Foundation

Before the derivations can be made, some general remarks are needed that lay the foundation for the transverse and longitudinal wave cut methods.

A steady flow is considered, and infinite water depth is assumed. A right hand Cartesian coordinate system is used, fixed to the ship. The x-axis is defined pointing upstream, and z points upward. A non-dimensional form is used for all parameters in this derivation. Length-related quantities will be normalized by the fundamental wavenumber.

$$k_0 = \frac{g}{U^2} \tag{3.11}$$

Wave resistance will be made non-dimensional by:

$$R_w = \mathbf{R_w} \frac{k_0^2}{\rho U^2} \tag{3.12}$$

Where $\mathbf{R_w}$ gives the dimensional wave resistance. Using the dispersion relation, the wave number k can be expressed as a function of the angle (θ) relative to the x-axis. For deep water, the dispersion relation gives $c^2 = \frac{g}{k}$. The wave should have the same speed as the model in the x direction, which gives $c = U\cos\theta$. This gives the (non-dimensional) relation:

$$k(\theta) = \sec^2\theta \tag{3.13}$$

The wave numbers in longitudinal (s) and transverse (u) direction can be given as:

$$s(\theta) = k(\theta)\cos\theta = \sec\theta \tag{3.14}$$

$$u(\theta) = k(\theta)\sin\theta = \tan\theta\sec\theta \tag{3.15}$$

It is also possible to write s as a function of u, using the fact that $u^2 + s^2 = k^2$ and that $k = s^2$. This results in:

$$s(u) = \sqrt{\frac{1+\sqrt{1+4u^2}}{2}} \tag{3.16}$$

From section 2.3, the linear wave elevation can be rewritten as a sum of multiple waves to represent the entire wave pattern:

$$\zeta(x,y) = \frac{1}{4\pi}\int_{-\infty}^{\infty} F(u)\sin(sx+uy) + G(u)\cos(sx+uy)\,du \tag{3.17}$$

Here, $F(u)$ and $G(u)$ are defined as the free wave spectrum and are only dependent on the transverse wave number u.

3.2.2. Transverse wave cut method

For a transverse wave cut, the wave elevation should be measured perpendicular to the ship's motion. It should be wide enough to capture all momentum flux. Therefore, it should extend outside the Kelvin wedge. The longitudinal position should not be too close to the hull, as near-field disturbance violates the linear assumptions of the analysis [22].

The first step in calculating wave resistance from wave elevation data is to determine the coefficients from the free wave spectrum. The transverse wave cut aims to obtain the coefficients F and G from two or more transverse wave cuts. F and G are needed for calculating the wave resistance as:

$$R_w = \frac{1}{16\pi}\int_{-\infty}^{\infty}\left[F(u)^2 + G(u)^2\right]\frac{\sqrt{1+4u^2}}{1+\sqrt{1+4u^2}}du \tag{3.18}$$

For the transverse wave cut, the wave pattern representation from Equation 3.17 will be written as:

$$\zeta(x,y) = \frac{1}{2\pi}\int_0^{\infty}\left[F_e(u)\sin(sx) + G_e(u)\cos(sx)\right]\cos(uy)\,du \tag{3.19}$$

$$+\frac{1}{2\pi}\int_0^{\infty}\left[F_o(u)\cos(sx) - G_o(u)\sin(sx)\right]\sin(uy)\,du \tag{3.20}$$

Here, the subscripts e and o denote the even and odd parts of F and G, respectively. For a wave cut $\zeta(x,y)$, where $x = \text{const}$, the Fourier transform is defined as:

$$C(u,x) + iS(u,x) = \int_{-\infty}^{\infty}\zeta(x,y)\,e^{iuy}dy \tag{3.21}$$

Using the Fourier inversion theorem, it can be seen that:

$$\begin{aligned} F_e(u)\sin(sx) + G_e(u)\cos(sx) &= 2C(u,x) \\ F_o(u)\cos(sx) - G_o(u)\sin(sx) &= 2S(u,x) \end{aligned} \tag{3.22}$$

This is a pair of linear equations with four unknowns. Using two wave cuts ($\zeta(x_1,y)$ and $\zeta(x_2,y)$), makes it possible to solve for F and G. The solution is given as:

$$\begin{aligned} F_e(u) - iG_e(u) &= \frac{2C(u,x_1)\,e^{isx_2} - 2C(u,x_2)\,e^{isx_1}}{\sin\left(s(x_1-x_2)\right)} \\ F_o(u) + iG_o(u) &= \frac{-2S(u,x_1)\,e^{isx_2} + 2S(u,x_2)\,e^{isx_1}}{\sin\left(s(x_1-x_2)\right)} \end{aligned} \tag{3.23}$$

Numerical difficulties can arise when the denominator $s(x_1-x_2)$ approaches a multiple of π. As s varies from $1 \leq s < \infty$, this is almost unavoidable. There are two ways to circumvent this. The first method is to use wave elevation and wave slope (ζ_x) for the same cut. Using the Fourier transform for both results in the following formula, where C_x and S_x are the Fourier constants of the wave slope:

$$iF_e(u) + G_e(u) = 2\frac{s\;C(u,x)\,e^{isx} + iC_x(u,x)\,e^{isx}}{s} \tag{3.24}$$

$$F_o(u) - iG_o(u) = 2\frac{s\;S(u,x)\,e^{isx} + iS_x(u,x)\,e^{isx}}{s} \tag{3.25}$$

For experiments, obtaining wave slope data is more difficult. The second method is to use more than two wave cuts. The system becomes overdetermined and can be solved using a least-squares solution. Another advantage of this method is that the effect of experimental error is reduced. In experimental setups, the number of wave cuts is limited by how many wave cuts can be measured. For calculated wave fields, Raven et al. (1998) [22] showed that using eight wave cuts worked well.

When the coefficients F_e, F_o, G_e, and G_o have been determined, the wave resistance can be calculated. Equation 3.18 can be rewritten to:

$$R_w = \frac{1}{8\pi}\int_0^\infty \left[F_e(u)^2 + F_o(u)^2 + G_e(u)^2 + G_o(u)^2\right] \frac{\sqrt{1+4u^2}}{1+\sqrt{1+4u^2}} du \tag{3.26}$$

This expression can be expanded for discrete values of the transverse wave number u for a wave cut with a finite width b. For $n = 0, 1, 2, ...$:

$$u_n = \frac{\pi n}{b} \tag{3.27}$$

Then the wave resistance formula is given in the following formula:

$$R_w = \frac{1}{8b}\sum_{n=0}^{\infty} \epsilon_n \left[F_e(u_n)^2 + F_o(u_n)^2 + G_e(u_n)^2 + G_o(u_n)^2\right] \frac{\sqrt{1+4u_n^2}}{1+\sqrt{1+4u_n^2}} \tag{3.28}$$

Here, ϵ_n is Neumann's factor and is defined as $\frac{1}{2}$ for $n = 0$ an 1 otherwise. This factor arises from the symmetry of the original integral. The full integral for R_w runs from $-\infty$ to ∞, which is folded to 0 to ∞ by exploiting symmetry. The value for $n = 0$ is half on the positive and half on the negative side of the bounds. To calculate only the positive contribution, a factor of 1/2 is introduced.

The wave resistance formula can also be rewritten in terms of θ. This results in a formula equivalent to that shown by Havelock (1934) [7]. A derivation of how this can be rewritten can be found in Appendix B.

Most subsequent research on transverse wave cut methods has been built on this method presented by Eggers, Sharma, and Ward (1967) [5]. This method has also been used by Mizuno and Wehausen (1966) [19] where they experimented with using stereophotographs for measuring the wave pattern.

Dependence of parameters

The process is dependent on a couple of parameters. One of these is the number of Fourier coefficients calculated. This depends on the resolution of the wave elevation data, since it only makes sense to include as many frequencies as there are data points. Increasing the sample size of the wave cut should add more wave components, thereby increasing accuracy.

Another parameter is the longitudinal location of the wave cut. Varying this should not matter, as the boundary of the momentum conservation should not affect the outcome. However, the width of the wave cut should be adjusted so that the entire wake is contained within the wave cut. For calculated wave fields, numerical damping can cause the wave resistance calculated by the wave cut method to decrease when the wave cut is located further behind. Prins and Raven (1998) [22] investigated how to circumvent this. They found that near-field disturbances from the hull are mostly negligible from 0.3 to 0.5 L_{pp} behind the stern.

The distance between the transverse wave cuts is also a parameter that can be varied in the analysis. Not much has been found in the literature about this.

3.2.3. Longitudinal wave cut method

This method uses a wave cut parallel to the flow direction. A longitudinal wave cut can easily be measured in experiments. A fixed probe can be placed in the water and measure the wave elevation as the ship passes.

The location of the wave cut depends mainly on three factors. The lateral distance, the usable length of the signal, and the speed or wave number. The first two influence each other in opposite directions. When the cut is close to the hull, the usable length is large, and the truncation is small. However, when the cut is too close to the hull, local wave effects have an effect. The location should therefore be as close as possible to the hull but far enough away so that local effects are reduced. Heimann (2000) [9] shows that stable results can be expected from $y/L_{pp} \approx 0.2$.

There are several publications about longitudinal wave cut (LWC) analysis. The most recent publication is by Heimann (2005) [10]. In this publication, a longitudinal wave cut is used, along with results from a panel method. He uses the method to optimize a hull. The longitudinal wave cut method [9] follows Sharma [23] and Eggers [5]. The method presented here follows Heimann and is applicable to deep

water. For more information on obtaining the wave elevation from experiments, Ward (1968) [26] can be consulted. ITTC guidelines for wave profile measurement (especially for longitudinal wave cut analysis) are also available [13].

The total wave field can be described as a function of the angle (θ).

$$\zeta(x,y) = \int_0^{\pi/2} \left[A(\theta)\cos(sx+uy) - B(\theta)\sin(sx+uy)\right]\, d\theta \tag{3.29}$$

It can also be written as a function of the longitudinal wave number k_x.

$$\zeta(x,y) = \int_1^{\infty} \left[A(s)\cos(sx+uy) - B(s)\sin(sx+uy)\right]\frac{d\theta}{ds}\, ds \tag{3.30}$$

Rearranging the terms gives:

$$\begin{aligned}\zeta(x,y) = \int_1^{\infty} &\left[\left(A(s)\cos(uy) + B(s)\sin(uy)\right)\cos(sx)\right. \\ &\left. + \left(B(s)\cos(uy) - A(s)\sin(uy)\right)\sin(sx)\right]\frac{d\theta}{ds}\, ds\end{aligned} \tag{3.31}$$

Now the Fourier transforms can be introduced as:

$$S(s) = \int_{-\infty}^{\infty} \zeta(x,y)\sin(sx)\, dx \tag{3.32}$$

$$C(s) = \int_{-\infty}^{\infty} \zeta(x,y)\cos(sx)\, dx \tag{3.33}$$

Here, S and C are the sine and cosine components of the Fourier transform. These can be filled in the following equation to obtain the full wave spectrum:

$$\zeta(x,y) = \frac{1}{\pi}\int_1^{\infty} \left[S(s)\sin(sx) + C(s)\cos(sx)\right]\, ds \tag{3.34}$$

The non-dimensional wave resistance can be calculated using the Fourier components:

$$R_w = \frac{1}{\pi}\int_1^{\infty} \left[S^2(s) + C^2 s)\right]\frac{1}{s}\sqrt{1-\frac{1}{s^2}}\, ds \tag{3.35}$$

It is possible to use the separated variables from Equation 3.31 and compare them with Equation 3.34. With this, a correlation between the components of the free wave spectrum and the Fourier transform can be found.

$$\begin{aligned}S(s) &= \pi\left(B(\theta)\cos(uy) + A(\theta)\sin(uy)\right)\frac{d\theta}{ds} \\ C(s) &= \pi\left(A(\theta)\cos(uy) - B(\theta)\sin(uy)\right)\frac{d\theta}{ds}\end{aligned} \tag{3.36}$$

Rearranging these for $A(\theta)$ and $B(\theta)$ gives:

$$\begin{aligned}A(\theta) &= \frac{1}{\pi}\left(C(s)\cos(uy) + S(s)\sin(uy)\right)\frac{ds}{d\theta}, \\ B(\theta) &= \frac{1}{\pi}\left(S(s)\cos(uy) - C(s)\sin(uy)\right)\frac{ds}{d\theta}\end{aligned} \tag{3.37}$$

This can be used to calculate the (non-dimensional) wave resistance using the formula from Havelock.

$$R_w = \pi\int_0^{\pi/2} \left[A^2(\theta) + B^2(\theta)\right]\cos^3(\theta)\, d\theta \tag{3.38}$$

In reality, the wave cut is limited by reflections of the tank wall or limited computer resources. Therefore, it needs to be truncated at a finite distance downstream. Upstream, this is not necessary because the wave effects decay fast enough. Far downstream, the wave pattern is largely dominated by transverse waves. Eggers et al. (1967) [5] suggested compensating for the error using an analytical asymptotic extension.

$$\zeta' \approx \frac{c_1 \cos x - c_2 \sin x}{\sqrt{c_3 + x}} \tag{3.39}$$

Coefficients $c_{1,2,3}$ are determined by fitting Equation 3.39 to the end of the wave cut signal x_E. A weighted Fourier transform can be used for determining the coefficients for the wave resistance for the domain $x_E \leq x < \infty$ as:

$$S'(s) = \int_{-\infty}^{x_E} \sqrt{(s)^2 - 1}\, \zeta'(x) \sin(sx)\, dx + \int_{x_E}^{\infty} \sqrt{(s)^2 - 1}\, \zeta(x, y) \sin(sx)\, dx \tag{3.40}$$

$$C'(s) = \int_{-\infty}^{x_E} \sqrt{(s)^2 - 1}\, \zeta'(x) \cos(sx)\, dx + \int_{x_E}^{\infty} \sqrt{(s)^2 - 1}\, \zeta(x, y) \cos(sx)\, dx \tag{3.41}$$

This can again be rewritten as components of the free wave spectrum:

$$A(\theta) = \frac{s}{\pi} \left(C'(s) \cos(uy) - S'(s) \sin(uy) \right) \tag{3.42}$$

$$B(\theta) = \frac{s}{\pi} \left(S'(s) \cos(uy) + C'(s) \sin(uy) \right) \tag{3.43}$$

In Heimann (2000) [9], he shows that wave pattern analysis from a calculated wave field is an appropriate tool because results correspond well with pressure integration. A spectral analysis as a function of θ can be made. The wave spectrum can give more information about the effect of the hull form on the wave field than pressure integration.

3.3. Spectral analysis

It is also possible to visualize the results of the wave pattern analysis. The integrand of the wave resistance formula can be plotted as a function of the transverse wave number. This way, the magnitude of each contribution for different transverse wave numbers can be visualized. It can be helpful to rewrite u as the wave angle (θ). It can be used to determine which wave angle contributes most to the wave resistance. This can give valuable insight into the cause of the wave resistance. It must be noted that it is not the amplitude of the wave that is obtained, but rather a degree of contribution to the wave resistance.

To obtain the wave angle from the transverse wave number (for a TWC), the relation given in Equation 3.15 between the transverse wave number and the wave angle can be rewritten as:

$$\theta(u) = \arctan\left(\pm \sqrt{-\frac{1}{2} + \frac{1}{2}\sqrt{1 + 4u^2}} \right) \tag{3.44}$$

For the transverse wave cut, the wave angle can range from $-90^\circ \leq \theta \leq 90^\circ$. As u ranges from 0 to N, the direction θ can be positive or negative. Therefore, the $\pm$ sign is applicable for this formula. For more information on this and on how to use it for longitudinal wave cuts, see the work of Heimann (2005) [10].

3.4. Side force

From the same coefficients of the free wave spectrum, the side force can be calculated. Sharma (1964) [24] showed, following a similar procedure as Havelock (1934) [7], that the side force can be found as:

$$F_y = \frac{\pi}{2} \int_{-\frac{\pi}{2}}^{\frac{\pi}{2}} [f^2(\theta) + g^2(\theta)] \cos^2(\theta) \sin(\theta)\, d\theta \tag{3.45}$$

For the transverse wave cut, where $f(\theta)$ and $g(\theta)$ consist of an odd and an even part, the formula can be rewritten as:

$$F_y = 2\pi \int_{0}^{\frac{\pi}{2}} [f_e(\theta) f_o(\theta) + g_e(\theta) g_o(\theta)] \cos^2(\theta) \sin(\theta)\, d\theta \tag{3.46}$$

This expression is written in terms of θ. To use this formula, the coefficients of the free wave spectrum should be calculated in terms of θ, or the equation should be rewritten in terms of the transverse wave number u.

Wave resistance is defined as the energy that flows from the ship to the waves (in longitudinal direction), divided by the speed at which the ship is sailing. Using the method described, the side force is defined the same way. It calculates the force acting on a ship due to the energy transfer to the waves in the transverse direction.

The publication of Sharma (1664) [24] was the only literature that has been found on the calculation of the side force. In this publication, no testing or validation has been done.

3.5. Comparison of transverse and longitudinal wave cut

Both methods have their advantages and disadvantages. Therefore, a comparison between the transverse and longitudinal wave cut methods will be made.

Starting with the integration bounds of both cuts. The advantage of a transverse wave cut is that the bounds are finite, as outside the Kelvin angle, the wave elevation quickly decays. To capture all momentum flux for a longitudinal cut, the cut should be infinite. In practice, this is not possible for experimental and computational methods. This is solved by using an error term to estimate this effect. If this term is used improperly, errors in the result can occur. In any case, the surface domain for the longitudinal wave cut is generally larger to capture most of the wave pattern.

The longitudinal wave cut can be measured more easily than a transverse wave cut. Probes fixed to a carriage must be used instead of a single stationary probe for the longitudinal wave cut. However, for calculated wave fields, this is no longer valid, because wave elevation data can be obtained in any direction.

As wave cut methods are based on a linear model, errors can be introduced when non-linear effects due to the viscous effects in the wake are measured. The transverse wave cut method uses wave elevation from this turbulent region. The longitudinal wave cut measures wave elevation outside the turbulent wake.

A minimum of two wave cuts is necessary for determining wave resistance with a transverse cut. For longitudinal wave cuts, one is sufficient (for symmetric flows). However, in most cases, multiple wave cuts will be used to reduce experimental error.

For calculated wave fields, especially with panel methods, the stern wave can be over-predicted. This error does not affect a longitudinal wave cut as much as it would affect a transverse wave cut.

3.6. Validity of the wave cut method

The wave-cut method is built on a linear wave model, which carries a number of underlying assumptions. The flow is assumed to be steady, inviscid, incompressible, and irrotational, allowing the use of a velocity potential. Additionally, the wave amplitude is assumed to be small relative to the wavelength, such that the free surface boundary conditions can be linearized and applied at $z = 0$ rather than at the true free surface $z = \zeta$. The upper integration bounds in the momentum integrals are also taken to $z = 0$ rather than $z = \zeta$. These simplifications are consistent in both models.

A direct consequence of the assumptions is that the method is not valid in the near-field region close to the hull. As discussed earlier in this report, the wave field in this region is dominated by nonlinear effects that linear wave theory cannot capture. Since the wave cut method is built on the assumptions of the linear wave model, it is equally invalid there. This is why it is required to measure the wave elevation sufficiently far from the hull for the wave cut, in a region where the flow is well described by linear wave theory.

The validity of the method also depends on the wave steepness of the generated wave pattern. When waves become too steep, for instance, at high ship speeds, the small amplitude assumption breaks down, and the linear model no longer accurately represents the physical wave field. Similarly, phenomena such as wave breaking and spray generation involve strongly nonlinear and viscous processes that fall entirely outside the scope of the method. Placing the transverse cut at a greater lateral distance from the hull can help reduce these effects, as the wave pattern has more space to spread and steepness is reduced, but in some cases, it does not eliminate the issue entirely. Care should be taken to verify that the wave field at the chosen cut location is consistent with the linearity assumption.

Finally, it is worth noting that a linear panel method is founded on the same set of assumptions as the linear wave model. Therefore, applying the transverse wave cut method to the results obtained from a linear panel code is consistent. So, as long as the ship and speed being simulated are reasonable for simulating with the panel method, the output is a valid input for the wave cut method. This consistency does not hold in general for CFD, where the flow is not assumed to be irrotational and inviscid, meaning the wave field may contain effects that fall outside the assumptions of the wave cut method. Results should be carefully inspected before applying the wave cut methods.

3.7. X-Y method

The 'X-Y' method is another way to determine wave resistance. It can be seen as a combined transverse and longitudinal method. It uses the horizontal force (X and Y) measurements from a long stationary cylinder placed in the flow off the tank centerline. This should represent the wave energy flux out of a control volume around the moving model.

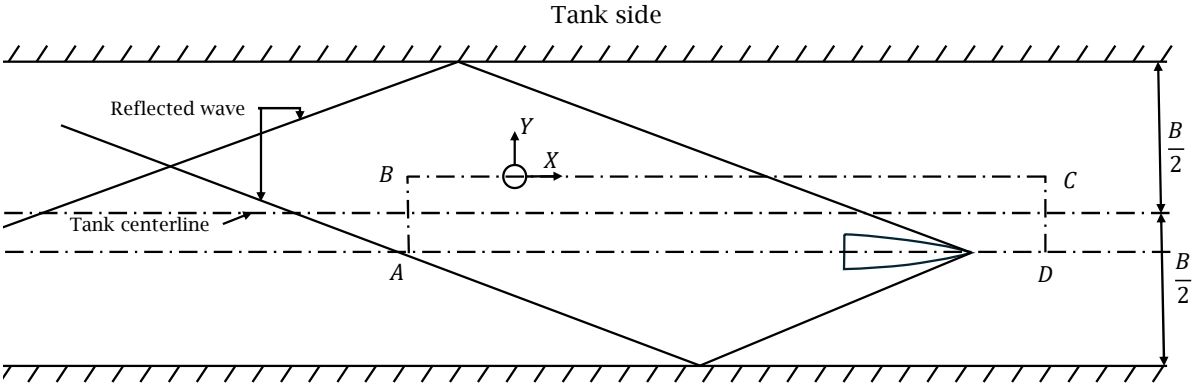

Figure 3.1: X-Y method setup

In Figure 3.1, a drawing of the setup for this method is shown. The cylinder moves across the line B-C and measures transverse and longitudinal forces. The forces acting on the cylinder are proportional to the wave height. By integrating the product of X and Y, a measure of energy flux across the line B-C is given. In the figure, the ship's path is placed off the centerline to enlarge the possible line B-C before the wave is reflected off the tank wall. The integral from the longitudinal wave cut will be:

$$\iint_{BC} \phi_x \phi_y \, dz \, dx = \frac{1}{2} \int_{BC} XY \, dx \tag{3.47}$$

The line A-B 'closes' the control box so that the reflection of the tank walls does not interfere. In region A-B, the wave is assumed to be a single component in the direction of the ship. This will be approximated by:

$$\frac{1}{2}\int_{AB}\zeta^2(x)\,dy + \iint_{AB}\phi_z - \phi_x\,dy\,dz = \frac{y}{2}\zeta_0^2 \tag{3.48}$$

Here, ζ_0 is the average amplitude, and y is the transverse location of the cut B-C. The expression for the wave resistance will be:

$$R_w = \frac{y}{2}\zeta_0^2 + \int_{BC} XY\,dx \tag{3.49}$$

For all quantities, a non-dimensional representation shall be used. The advantage of this method is that it is very simple, and it is not necessary to evaluate Fourier transforms. This method works for symmetric and asymmetric flows, but for asymmetric flows, a cylinder needs to be placed on each side. The disadvantage is that the X-Y forces on the cylinder need to be calibrated, and that it is less accurate than previously described methods. The explanation can be found in papers from Eggers ([5] and [2]). A more complete explanation could be found in Ward (1963) [25].

4

Methodology

This chapter describes how the transverse wave cut used to obtain the side force is implemented and tested. First, the implementation of the transverse wave cut is given. After this, the numerical setup is presented, and the test subjects are given. Finally, validation of the transverse wave cut method will be presented.

4.1. Transverse wave cut method for determining side force

A transverse wave cut will be used to calculate the side force acting on the body in a uniform flow, and is chosen over a longitudinal wave cut method, as this is considered more suitable for this purpose.

The transverse wave cut is preferred mainly because it has finite integration boundaries, in contrast to the longitudinal wave cut. No error term is needed for the extension of the signal. It is expected that the integral form of the longitudinal wave cut is a subtraction of the momentum of the port side boundary from the starboard boundary. This was also the case for the wave resistance from a longitudinal wave cut from the momentum analysis in Appendix A. As the bounds are infinite, it can create difficulties when the information about the wave pattern is only finite.

The longitudinal wave cut has the advantage that only one wave cut is required, but for asymmetric wave fields, wave cuts on both sides are needed. Although longitudinal wave cuts are easier to measure, this advantage disappears for calculated wave fields, as wave elevation can be obtained in any direction.

From the literature, two main methods emerged for calculating the side force from a transverse wave cut. The first method is to evaluate the integral formula from the momentum conservation. This requires perturbation velocities obtained from a numerical fluid analysis. The second method is to use a Fourier transform method, which makes it possible to calculate the side force using only wave elevation data.

For both methods, it is important to use the transverse wave cut with an appropriate width. This is because the entire wave pattern should be contained in the wave cut. Waves spread outward behind a moving vessel at the characteristic Kelvin wake angle. The Kelvin angle can be used to calculate the minimum width required for different longitudinal wave cut locations.

4.1.1. Integral formula

In subsection 2.5.3, an expression for the side force from a transverse cut was derived. This is shown below and forms the foundation of the Fourier transform method. It is also possible to directly evaluate it using perturbation velocities obtained from a computational fluid model.

$$F_y = \rho \int_{-b/2}^{b/2} \int_{-h}^{\zeta} (U + \phi_x)\phi_y \, dz \, dy \tag{4.1}$$

This method has been implemented in the panel method based on the Neumann-Kelvin source panel. In this environment, it is possible to calculate velocities at any point in the field. The double integral is

evaluated using a double Gaussian quadrature method.

Results for this method are not as expected. The results are generally much lower than the pressure integration results. The direct integration of the wave resistance formula yields results similar to pressure integration. An explanation for why the side force gave incorrect results, while the resistance was calculated correctly, was not found. Therefore, this method will not be tested further. The results can be found in Appendix D.

4.1.2. Fourier method

In subsection 3.2.2, it was shown how the coefficients from the free wave spectrum can be calculated. After this, the coefficient can be used to determine the wave resistance or the side force. The side force formula that was given in a publication from Sharma [24] was given in the wave angle (θ) domain. Using the relations between the transverse wave number u and the wave angle, it was rewritten in the u-domain. It is based on a similar transformation of the wave resistance formula from the Fourier transform method, which can be read in Appendix B. By rewriting it, it can be used with the same coefficients of the free wave spectrum. The transformation of the side force formula is shown in Appendix C. The result is as follows:

$$F_y = \frac{1}{16\pi}\int_{-\infty}^{\infty}[F^2(u)+G^2(u)]\frac{u\sqrt{1+4u^2}}{1+\sqrt{1+4u^2}}\sqrt{\frac{2}{1+\sqrt{1+4u^2}}}\,du \tag{4.2}$$

For a transverse wave cut, the coefficients F and G consist of an odd and even component, noted with subscripts e and o. Writing out the coefficients gives:

$$F^2(u)+G^2(u) = F_e^2(u)+2F_e(u)F_o(u)+F_o^2(u)+G_e^2(u)+2G_e(u)G_o(u)+G_o^2(u) \tag{4.3}$$

Integrating an odd function over a symmetric domain gives zero as an answer. The factor after the coefficients is an odd function. Therefore, when it is multiplied with the even functions $F_e^2(u)$, $F_o^2(u)$, $G_e^2(u)$ and $G_o^2(u)$, it results in zero. For the multiplication of the odd functions $2F_e(u)F_o(u)$ and $2G_e(u)G_o(u)$, an even function will be obtained. All this will result in the following formula for the side force.

$$F_y = \frac{1}{4\pi}\int_{0}^{\infty}[G_e(u)G_o(u)+F_e(u)G_o(u)]\frac{u\sqrt{1+4u^2}}{1+\sqrt{1+4u^2}}\sqrt{\frac{2}{1+\sqrt{1+4u^2}}}\,du \tag{4.4}$$

For a discrete set of transverse wave numbers u_n, the formula can be written as:

$$F_y = \frac{1}{4b}\sum_{n=0}^{\infty}\epsilon_n\left[G_e(u_n)G_o(u_n)+F_e(u_n)G_o(u_n)\right]\frac{u_n\sqrt{1+4u_n^2}}{1+\sqrt{1+4u_n^2}}\sqrt{\frac{2}{1+\sqrt{1+4u_n^2}}} \tag{4.5}$$

Here ϵ is (just as with the resistance) defined as $\frac{1}{2}$ for $n=0$ and 1 otherwise. To obtain the dimensional side force ($\mathbf{F_y}$), it should be scaled back to dimensional numbers:

$$\mathbf{F_y} = F_y\frac{\rho U^2}{k_0^2} \tag{4.6}$$

Now that the force formula has been derived, only the coefficients of the free wave spectrum need to be determined. This has been done following the paper by Eggers, Sharma, and Ward (1967) [5], and can be read in subsection 3.2.2. The derivations are based on non-dimensional values. A short, more specifically tailored version will be given here.

The Fourier coefficients C and S for each wave cut at x_i are determined by using a Simpson integration technique. Discrete values of the transverse wave number u will be used for each integration. u will be given as $u_n = \frac{\pi n}{b}$, for $n = 0, 1, 2\ldots$. The number of frequencies, n, depends on the grid points.

$$C(u_n,x_i)+iS(u_n,x_i) = \int_{-b/2}^{b/2}\zeta(x_i,y)\,e^{iu_n y}dy \tag{4.7}$$

The longitudinal wave number $s(u)$ is written as a function of u and is given as:

$$s(u) = \sqrt{\frac{1+\sqrt{1+4u^2}}{2}} \tag{4.8}$$

For each u_n, the following pair of linear equations can be solved to obtain the F and G coefficients. It must be noted that this system has four unknowns and two equations. Therefore, at least two wave cuts are needed to solve the system of equations.

$$\begin{aligned} F_e(u_n)\sin(sx_i) + G_e(u_n)\cos(sx_i) &= 2C(u_n, x_i) \\ F_o(u_n)\cos(sx_i) - G_o(u_n)\sin(sx_i) &= 2S(u_n, x_i) \end{aligned} \tag{4.9}$$

Solving this system can be done using a numerical solver, or using these expressions:

$$\begin{aligned} F_e(u_n) - iG_e(u_n) &= \frac{2C(u_n, x_1)\, e^{isx_2} - 2C(u_n, x_2)\, e^{isx_1}}{\sin\left(s(x_1 - x_2)\right)} \\ F_o(u_n) + iG_o(u_n) &= \frac{-2S(u_n, x_1)\, e^{isx_2} + 2S(u_n, x_2)\, e^{isx_1}}{\sin\left(s(x_1 - x_2)\right)} \end{aligned} \tag{4.10}$$

For this TWC method, three different parameters can be varied. First, the number of Fourier coefficients can be changed if more or fewer grid points are available. The longitudinal location of the wave cut can also be varied. It should be sufficiently far away from the hull to reduce near-field effects. The location of the wave cut should, in theory, not have an influence on the outcome of the result as long as it is located sufficiently far away from the hull and the cut is wide enough to capture the full width of the wave pattern. The distance between the wave cuts is also a parameter that can influence the outcome. The effect of this needs to be studied.

4.1.3. Matrix method

When more than two wave cut methods are used, the system of equations becomes Equation 4.9 overdetermined. The system can then be written as Equation 4.11. In that case, the system can be solved using a least squares method. In the literature, this is often referred to as a matrix method. From Equation 4.10, it can be seen that certain numerical difficulty arises when $s(x_1 - x_2)$ approaches a multiple of π. This can be circumvented by using the least squares method. Another advantage is that it can reduce experimental error.

$$\begin{bmatrix} \sin(sx_1) & \cos(sx_1) & 0 & 0 \\ 0 & 0 & \cos(sx_1) & -\sin(sx_1) \\ \vdots & \vdots & \vdots & \vdots \\ \sin(sx_i) & \cos(sx_i) & 0 & 0 \\ 0 & 0 & \cos(sx_i) & -\sin(sx_i) \end{bmatrix} \begin{bmatrix} F_e(u_n) \\ G_e(u_n) \\ F_o(u_n) \\ G_o(u_n) \end{bmatrix} = \begin{bmatrix} 2C(u_n, x_1) \\ 2S(u_n, x_1) \\ \vdots \\ 2C(u_n, x_i) \\ 2S(u_n, x_i) \end{bmatrix} \tag{4.11}$$

4.1.4. Spectral analysis

In section 3.3, spectral analysis for the wave resistance is discussed. For the side force, the same analysis can be done by plotting the integrand of the side force formula as a function of the wave angle. As seen previously, the integrand is calculated as follows:

$$C_y(u_n) = \frac{1}{4\pi}\epsilon_n \left[G_e(u_n)G_o(u_n) + F_e(u_n)G_o(u_n)\right] \frac{u_n\sqrt{1+4u_n^2}}{1+\sqrt{1+4u_n^2}} \sqrt{\frac{2}{1+\sqrt{1+4u_n^2}}} \tag{4.12}$$

For each u_n, the contribution to the side force can be calculated. When each contribution is multiplied by $du = \frac{\pi}{b}$, the total force can be found. It would make more physical sense to use the wave angle instead of the wave number. Equation 3.44 can be used to transform the wave number to the wave angle.

For the resistance force, a similar analysis can be done. In that case, it proved to be a very useful tool, providing a chart of wave directions that shows the contribution to the wave resistance. This can be used to help make alterations to a hull design to minimize the resistance. For the side force, the goal is not always to minimize the force, but rather to calculate it accurately. Results will show if wave spectrum analysis is a useful tool in this case. In any case, something can be learned by comparing the wave resistance spectrum with the side force spectrum.

4.2. Test cases

Two different test bodies were tested. The results were validated using pressure integration.

4.2.1. Submerged Spheroid

The first test body is a submerged prolate spheroid. This is considered the simplest case. The shape can easily be parametrized, and it does not pierce the free surface. The body must be close to the surface, as otherwise no waves are generated. This reduces the total error that can come from a linear panel method. When not specified, the Froude number at which it will be tested is 0.5. The main dimensions and the Froude number are given in Table 4.1. With the spheroid at a depth of $1/8$, and radius of $1/12$, a $1/24$ m gap exists between the free surface and the body.

Main parameters		
L	1	m
Beam	$1/6$	m
Z (z-translation)	$-1/8$	m

Table 4.1: Main parameters of the spheroid

4.2.2. Ecoliner

The next step is to test a surface-piercing hull. A wind-assisted ship is a relevant test case because side forces are often present under wind-assisted conditions. Therefore, a ship from the Delft Wind Assist series is used. The Delft Wind Assist series is a set of 60 hulls developed at the TU Delft. These are based on the design of the Ecoliner by Dykstra Naval Architects [27]. The 138 meter long Ecoliner parent hull is used for testing. An advantage of this hull is that it has no gondola stern, which makes meshing easier. The main parameters of the ship can be found in Table 4.2.

Main parameters	Full scale	Model scale ($1:50$)	
L_{pp}	138	2.76	m
Beam	18	0.36	m
Draft	6.5	0.13	m
Displacement	11597	0.09278	m^3
LCB	50.13	50.13	%

Table 4.2: Main parameters of the Ecoliner

Figure 4.1: Ecoliner parent hull [27]

For the CFD-simulation of the Ecoliner, the ship has been tested at $\beta = 3°$. This is considered a realistic angle at which the ship will operate. In previous research regarding the Ecoliner [16], three velocities were considered: Fn = 0.128, 0.168, and 0.210. This corresponds to 9, 12, and 15 knots at full scale. The highest speed was chosen for testing in this study because it would cause higher waves.

4.3. Numerical setup

Numerical calculations must be done to obtain the wave elevation. Both volume-flow methods and panel methods have been considered. Two numerical methods were available for this project. Firstly, a panel method is used because it is not as computationally expensive. The Fourier method previously described is based on linear frictionless waves, while panel methods are also based on frictionless potential flow; this makes it suitable to work with. After this, results from a volume-flow method will be used to further test the method. For this, the open-source CFD program OpenFOAM is used.

For both methods, sinkage and trim are not considered, and deep water is assumed. Symmetry planes can often be used to speed up calculations. For asymmetric flow, this is not possible, so this cannot be used. The x-axis is defined positive in the direction of travel, the y-axis is defined positive to the port side, and the z-axis is pointing upwards. This is consistent with the orientation of Eggers, Sharma, and Ward (1967) [5].

4.3.1. Julia - NeumannKelvin

This panel method is based on Neumann-Kelvin source panels and is written in the programming language Julia by Gabe Weymouth. This is a linear method using only source panels on the body. The Neumann-Kelvin source panels automatically satisfy the free surface boundary condition. Therefore, no free surface panels are needed. As there are fewer panels (no surface panels), flow properties can be calculated very fast anywhere in the field using the influence of all of the panels. This makes it possible to be flexible in the calculation of the wave elevation data and choose the grid points and spacing. This also makes it possible to compute the perturbation velocities needed to evaluate the integral equation for the side force.

For surface piercing hulls, the Neumann-Kelvin method is less accurate. This is due to the nature of the panel. Near the free surface, the panel generates waves with $\lambda \to 0$, while the amplitude remains constant, creating infinite slope waves. These can not be integrated accurately, and the solution is to neglect small wavelengths. One of the originators (F. Noblesse) of the Green's function of this method admitted that this is still an open problem. Therefore, a fully submerged spheroid will be used for testing.

The panel method calculates the forces acting on the hull by integrating pressure. This value represents the wave resistance, since no viscous forces are involved. Therefore, the result of the pressure integration can be used to verify the wave cut method.

4.3.2. OpenFoam

OpenFOAM is used to test the TWC method for wave fields obtained by volume methods. OpenFOAM is a free, open-source CFD software. It is very versatile and can be used for many applications. In this case, the method InterFOAM is used to account for the air-water surface interface. The turbulent flow is modeled by solving the Reynolds-Averaged Navier-Stokes (RANS) equations. The ship will be sailing through undisturbed water, so a steady flow is simulated. No sinkage and trim is considered.

This method also calculates the forces on the hull. The pressure and viscous components are integrated over the hull, and the total force can be obtained from the method. It must be noted that the pressure force includes viscous pressure effects. The calculated pressure force is therefore not the same as the wave resistance.

CFD simulations generally take much longer to compute than panel methods. To reduce computation time, the supercomputer DelftBlue is used to speed up calculations. The TU Delft designs Delftblue for research purposes.

In most CFD cases, important flow components are close to the hull. For the calculation of forces by integration, only near-field effects are considered. Also, for propeller wake analysis, flow near the propeller or close to the hull is of interest. For a transverse wave cut, the interest is more in the far field. Measures must be taken to ensure that the wave does not damp out more quickly than in reality.

Meshing is an important aspect in every CFD simulation, and it is also important in this case. First, a simulation will be done using some standard settings for ship hydrodynamics. Results for this will be shown, and the TWC method will be tested on this result. Most simulations are set up for calculating near-field forces or visualizing flow near the hull. The wave field behind the ship is usually of less interest. It will be interesting to see how the TWC method behaves for this case when no adjustments have been made. A second simulation will be done to determine whether certain adjustments can be made to better suit the CFD simulation for a TWC analysis. Version 2 will aim to optimize the CFD parameters to create a result that more accurately describes the wave pattern behind the ship. The parameters of the two versions will be given in the next sections.

Version 1

The steady-state simulation is solved using the interFoam solver in OpenFOAM. This enables simulation of the interface between two fluids using the PIMPLE algorithm. The LocalEuler time scheme was used. As for steady-state simulation, this method is considered to efficiently converge to the solution. The k-ω Shear Stress Transport (SST) RAS turbulence model is used. This model has proven to give accurate predictions for ship hydrodynamics and is the most widely used model in this field [12]. For the near-wall modeling, a wall function is used. This eliminates the need for very fine refinements near the wall. The y^+ value is put at 60.

The ship's meshing is performed using OpenFOAM's SnappyHexMesh utility. Hexahedral cells are mostly used, and a structured mesh is generated. The mesh is aligned with the undisturbed flow, and a mesh check is performed to filter out poor mesh quality. All this is done to reduce the numerical diffusion induced by the discretization. In the mesh, different refinement regions are inserted for accuracy in certain areas:

- Bow
- Stern
- Transom
- Kelvin wake
- Free Surface

The Ecoliner will be used for the CFD simulations. Figures of the mesh are shown in Figure 4.2. In the figures, the different refinement regions can clearly be identified. Furthest away from the hull, the mesh is the largest. This is to ensure that the disturbances dampen out, as larger cell sizes introduce more wave damping. It is important to mesh the Kelvin angle with a finer cell resolution to ensure that the wave field is accurately simulated and that numerical damping is minimized. In Figure 4.2b,

the boundary layer can be seen. It shows that the boundary layer is parallel to the ship and that the distance between cells gradually increases. In total, the mesh has 1.9 million cells.

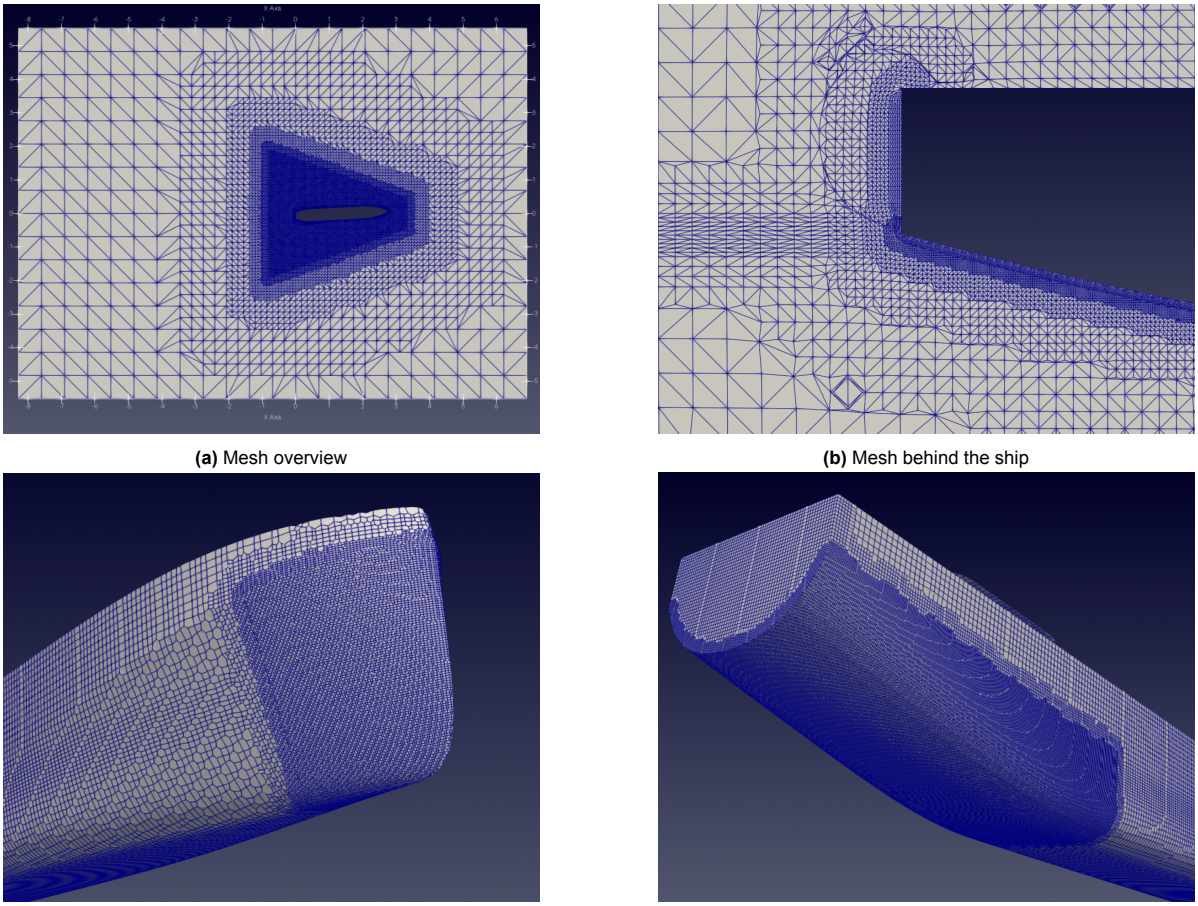

(a) Mesh overview

(b) Mesh behind the ship

(c) Mesh refinement on the bow

(d) Mesh refinement on the stern

Figure 4.2: Meshing of the Ecoliner version 1

Version 2

Most of the parameters of version 1 have not been changed. The parameters that have been changed will be discussed here. Each adjustment aims to improve the quality of the wave pattern behind the ship.

Firstly, the localEuler time scheme replaces the Euler method. Both time schemes are first order. localEuler uses a pseudo time stepping scheme and is designed to achieve fast convergence for steady flow cases. The Euler time scheme uses a physically accurate timestep. This method was found to give more detail (for example, in the turbulent wake area) [14]. Switching to this method will hopefully help describe the wave pattern more accurately.

The refinement regions have also been changed. The Kelvin angle has been extended, resulting in a slower decay of the wave pattern. This is helpful for the TWC method, as the longitudinal location of the TWC can be evaluated at a further distance away from the hull. In version 1, the Kelvin wake refinement ended at $0.3L_{pp}$ behind the hull. This has been elongated to $0.6L_{pp}$. Expanding this further caused the computation to exceed the supercomputer's maximum allowed runtime. The kelvin refinement region can be seen in Figure 4.3. A turbulent wake refinement region has been added to better simulate the area near the ship. This would not have much effect on the wave damping, but would give an improvement in the generation of the waves. These adjustments increased the number of cells. In version 1, 1.9 million cells are used; in version 2, 3.8 million cells are used. The Euler time scheme converged more slowly than the localEuler scheme. Combined with the increase in cells, this increases the duration of the simulation.

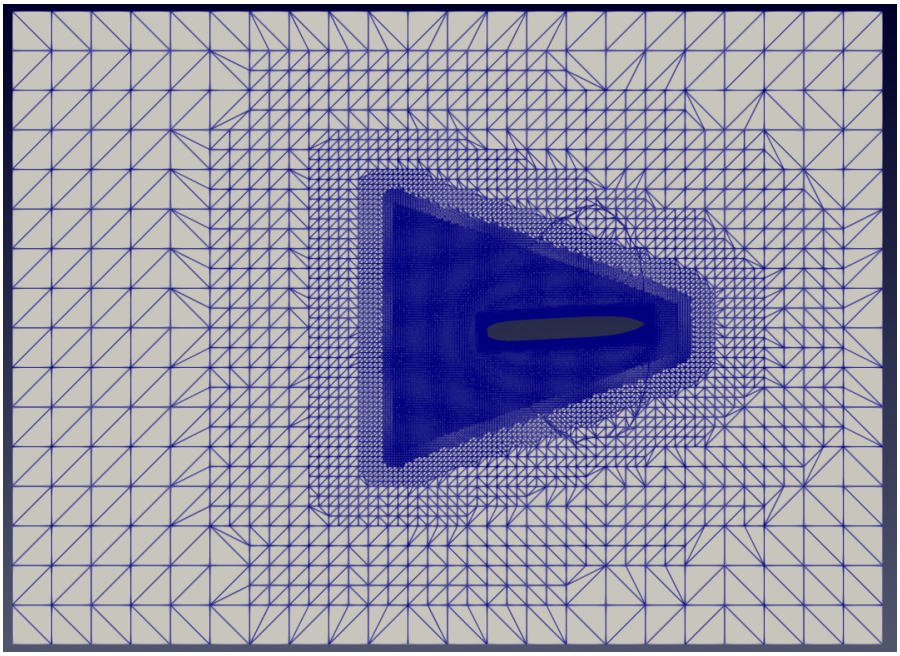

Figure 4.3: Kelvin wake refinement of version 2

Postprocessing

After the simulation is complete, the results can be viewed in ParaView. For the wave cut method, the wave field is exported from ParaView and saved as a CSV file. This is read using a Python file. As wave elevation data is not equally spaced, a 2D-linear interpolation will be used to obtain the wave field at equally spaced intervals. This also makes it possible to choose the distance between the wave cuts and the number of wave cuts.

4.4. Validation

The method for obtaining the side force is essentially calculating the force due to the transfer of energy from the ship to the waves in the transverse direction. For inviscid flow, this force should be similar to the force obtained from pressure integration. In this section, the previously described method is validated by comparing it with the pressure integration results from the Neumann-Kelvin panel method.

The submerged spheroid test case is used, as this is the most basic test case. Other test cases may introduce errors induced by circulation or surface-piercing effects. The main parameters are described in Table 4.1 and for this case the drift angle $\beta = 10°$, unless specified otherwise. The resulting wave field for the submerged spheroid can be seen in Figure 4.4.

For all results, the non-dimensional force coefficient is used for comparison. Here, S denotes the wetted surface area in the stationary and floating positions.

$$C_i = \frac{F_i}{\frac{1}{2}\rho U^2 S} \tag{4.13}$$

Two transverse wave cuts (TWC) are used, so no least squares approximation is used. The Neumann-Kelvin Julia panel method is used, which allows choosing the spacing between grid points. This also determines how many wave components are included. When unspecified, 80 wave components are included. A relatively fine grid is used, consisting of 624 panels. The distance between the wave cuts is set at $0.2\ m$.

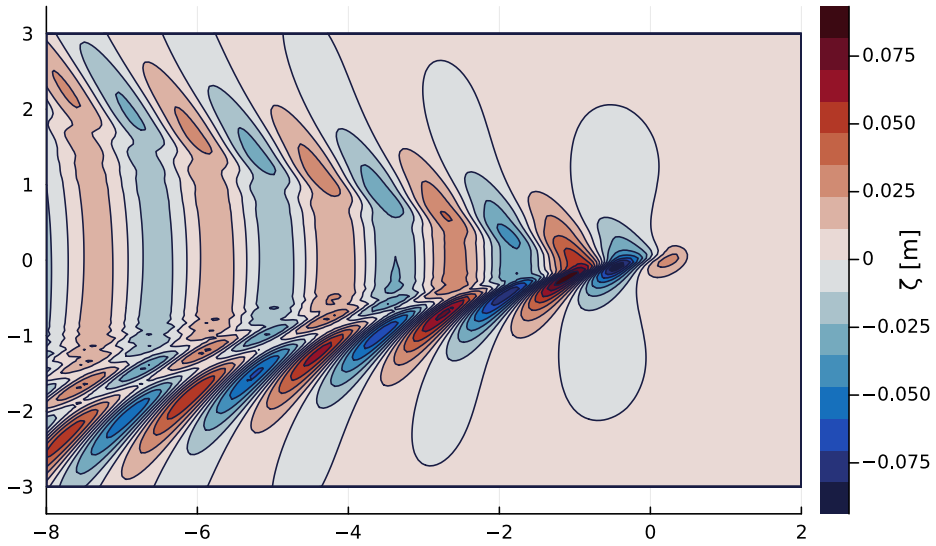

Figure 4.4: Wave elevation

4.4.1. Validation of the panel method

The pressure integration from the panel method should be validated before the calculated side force is compared to the results obtained from pressure integration. For the spheroid under drift, no data has been found to compare the results and validate the method. However, an analytical solution for the spheroid with no drift angle is available and was presented by Farell (1973). This result can be used to validate the pressure integration of the panel method. In Figure 4.5, the wave resistance coefficients are compared with the pressure integration and TWC results for different Froude numbers.

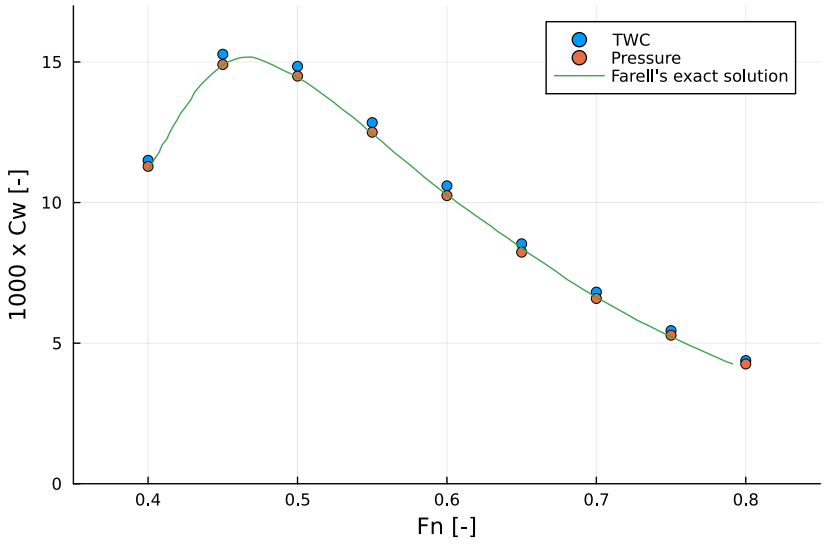

Figure 4.5: Wave resistance compared with Farell's exact solution [6]

It can be seen that the pressure integration result corresponds accurately with Farrell's exact solution. From this, it can be assumed that the results from this panel method are valid. Secondly, the results show that the wave resistance calculated by the wave cut method is very close to both solutions. The TWC method is largely the same for the side force, as the calculation of the Fourier coefficients is the

same. Therefore, it can be concluded that the calculation of the coefficients is correct.

4.4.2. Longitudinal position of TWC

A first check to confirm the validity of the method is to vary the longitudinal position of the wave cut. As long as the wave cut is wide enough, this should result in the same force. Only very close to the hull, non-linear near-field effects can be expected, which can cause errors in a linear model. In Figure 4.6, the side force for the different x-locations can be seen. The pressure integration result has also been plotted.

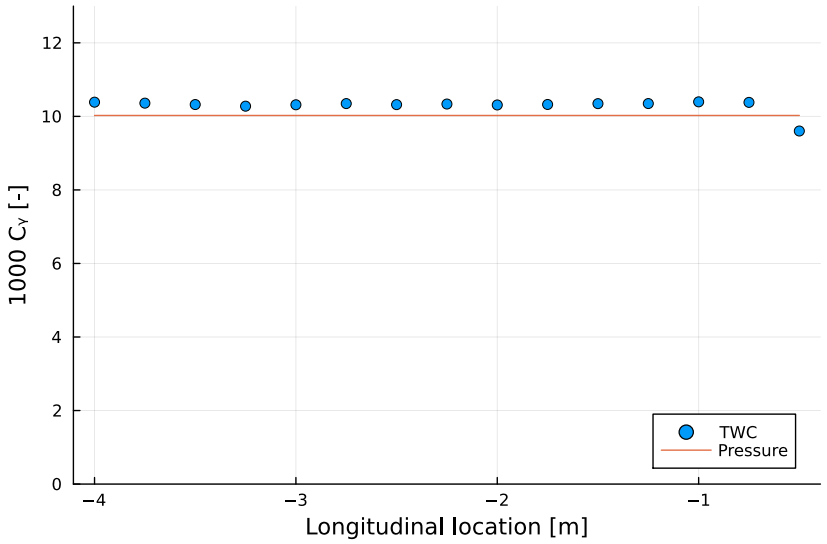

Figure 4.6: Side force for different longitudinal positions of the TWC

The side force calculated by the TWC is very consistent for different locations. The only difference is when the location is right behind the hull. At $x = -0.5$, a small deviation can be seen. This is probably the case, as near-field effects influence the wave pattern. Here, the wave pattern cannot be captured with a sum of linear regular waves. Prins and Raven (1998) [22] found that near-field effects are negligible from 0.3 to 0.5 L_{pp} behind the stern. In this case, the near-field effects are negligible even closer to the stern.

The pressure integration results are constant, as they do not depend on location. Overall, the results from the pressure integration are only slightly lower than the transverse wave cut.

4.4.3. Grid convergence

To assess whether the transverse wave cut method converges with more panels, a quick grid-convergence study can be conducted. In Figure 4.7, the side force calculated by the TWC and pressure integration for an increasing number of panels can be seen. Note that the x-axis is showing a logarithmic scale.

For increasingly fine grids, it can be seen that both methods converge to the same value. This means that the TWC is consistent with the side force obtained from pressure integration. As a result of the longitudinal position of the TWC, it could be seen that the pressure integration was slightly lower than the TWC method. The differences were most likely caused by using too few panels, as this result shows that increasing the resolution reduces the difference.

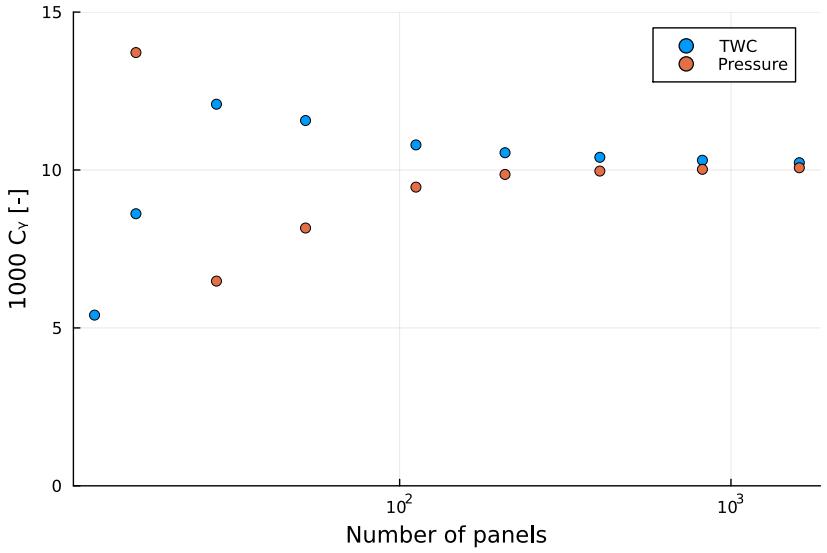

Figure 4.7: Grid convergence

4.4.4. Number of frequencies

The next test is to determine whether the method converges when more frequencies of $u_n = \frac{\pi n}{b}$ are added. The number of frequencies depends directly on the free surface grid spacing. The number of grid points can easily be adjusted in the Neumann-Kelvin panel method. It is expected that the side force converges as the number of frequencies increases. In Figure 4.8, the relation can be seen.

After roughly 60 frequencies, the side force stabilizes. Beyond this, adding more frequencies does not give notable changes to the side force. Overall, it shows a clear convergence. It converges to a value that is slightly higher than the pressure integration. Again, the differences are most likely caused by using too few panels, which was shown in the grid convergence study.

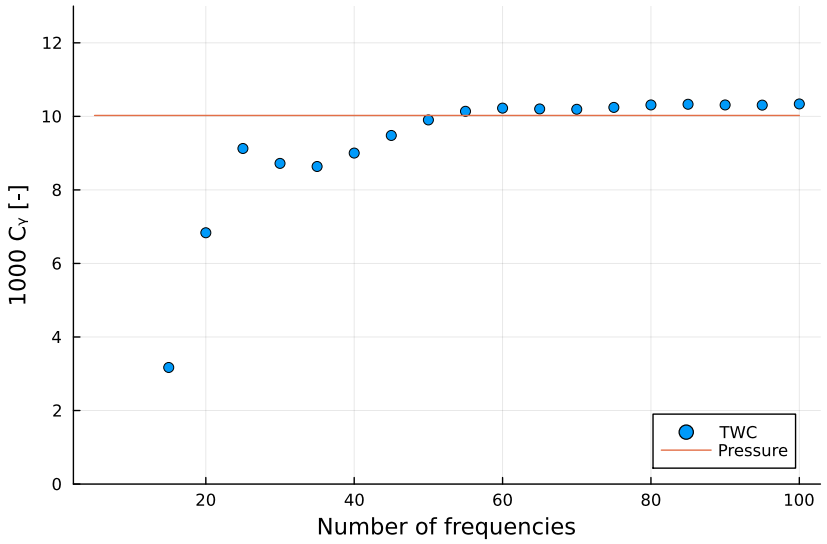

Figure 4.8: Side force for number of frequencies

4.4.5. Velocity

Increasing the spheroid's velocity will change the side force. The result for the wave resistance was already shown, but for the side force, it can be seen in this section. In Figure 4.9, it can be seen that

the force corresponds very well to the pressure integration. The plot shows only Froude numbers from 0.3 onward, as no waves are generated below that speed, resulting in no wave forces.

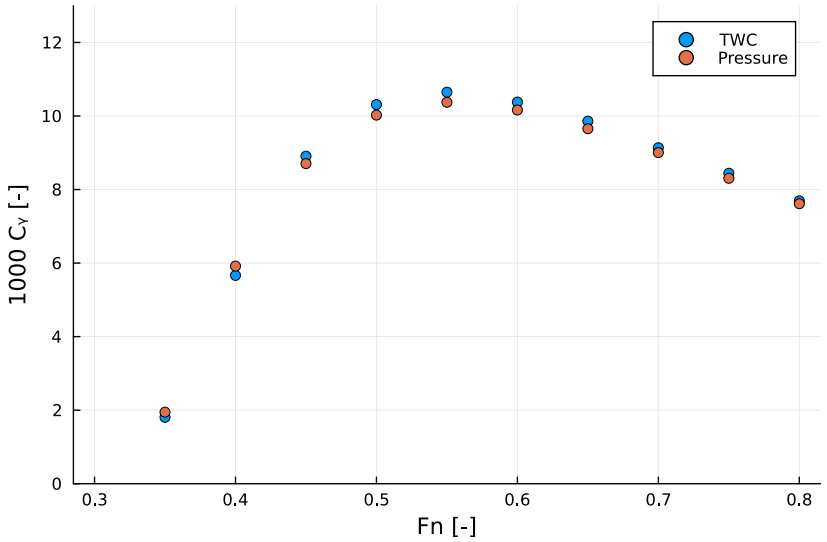

Figure 4.9: Side force for different Fn

4.4.6. Angle

The final plot for validation shows how the side force varies with different leeway angles β. The angle ranges from $0°$ to $-90°$. In Figure 4.10, the result can be seen. The side force is expected to be zero at $\beta = 0°$ and $\beta = 90°$, because the spheroid is symmetric to the xz-plane. Overall, both methods correspond really well, even for very large angles.

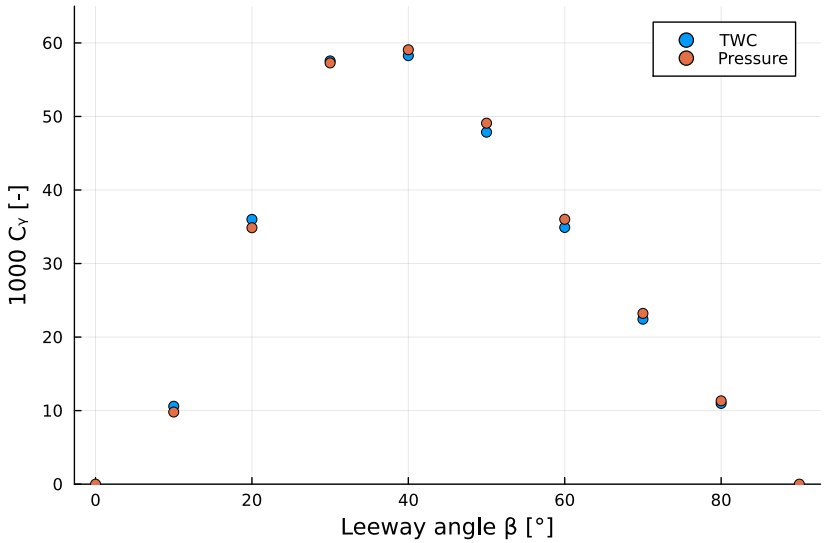

Figure 4.10: Side force at different leeway angles

4.4.7. Conclusion

The TWC method was validated with several checks. First, it was shown that the panel method correctly calculates the force on the Spheroid using Farell's exact solution. It was demonstrated that the wave cut is consistent for different longitudinal locations. After this, the grid convergence study showed that for high panel density, the pressure integration and TWC methods converge to the same value. Next,

it was confirmed that the method converges when more wave components are added. Finally, it was shown that both forces are equal across different Froude numbers and drift angles. For the simple non-surface-piercing spheroid, it can be concluded that the implementation of the TWC is consistent with pressure integration and is numerically stable.

5

Results and Discussion

In this section, the results will be displayed and discussed. Results will be generated according to the methodology. First, some results for the submerged spheroid simulation using the panel method will be discussed in section 5.1. After this, the results of the Ecoliner simulation in OpenFOAM will be discussed and presented in section 5.2.

5.1. Submerged Spheroid - Panel Method

In the validation case, results for the submerged spheroid model have been given for different speeds, panel sizes, angles, and the number of frequencies. However, two variables that are embedded in the TWC method have not yet been shown. This is because it is not so much a validation case, but more a result of how the method behaves for different parameters. In this section, some results for the submerged spheroid are presented.

5.1.1. Wave cuts properties

Up to now, only two wave cuts have been used to obtain the side force on the submerged spheroid. The distance between the cuts can be changed. Figure 5.1 has been made to see how this changes the result.

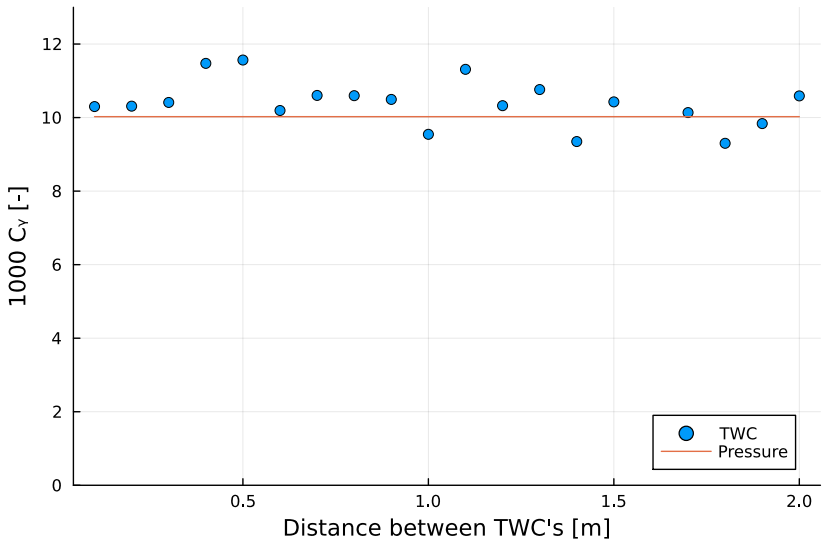

Figure 5.1: Side force plotted over the distance between the wave cuts

It can be seen that for values lower than 0.3, the results are relatively constant. After this, the results

vary widely. Inconsistencies in the outcome can also be found in other papers. This is because the denominator of Equation 4.10 tends to zero, leading to peaks when calculating the coefficients. The literature showed a way to solve this: to solve the system 4.9 using a least-squares approximation with more than two wave cuts.

Number of wave cuts

The largest error is for a distance of $0.5\ m$ between the wave cuts. Using the flexibility of the Neumann-Kelvin panel method in Julia once more, it is possible to calculate multiple wave cuts at chosen intervals. For the worst case ($dx = 0.5\ m$), the influence of using more wave cuts is investigated in Figure 5.2.

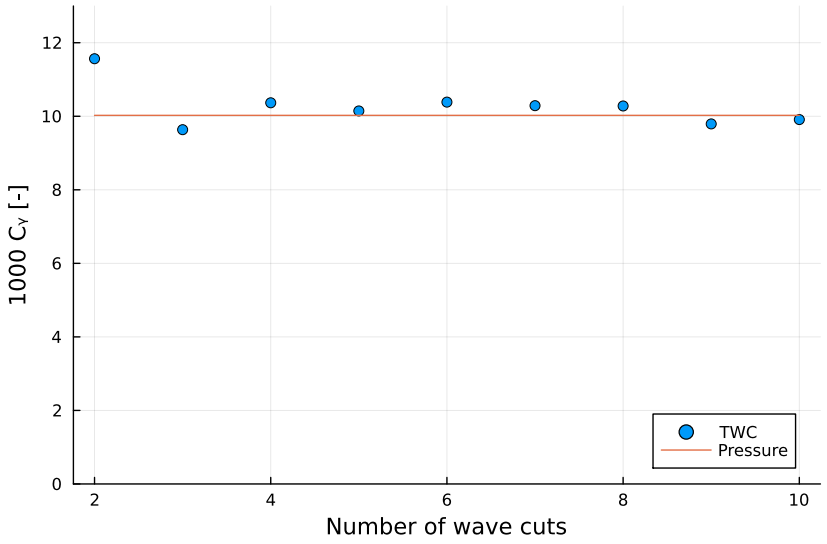

Figure 5.2: Side force plotted over the number of wave cuts

For two wave cuts, the result is the same as in Figure 5.1. After this, the side force converges to the pressure integration value, indicating that using more wave cuts gives more stable results.

To confirm this, the distance between the wave cuts can be replotted for 8 wave cuts. This number has been chosen as it is recommended by Prins and Raven (1998) [22]. The result can be seen in Figure 5.3. The distance between the first and last wave cuts has remained similar, so more wave cuts are added at equal spacing in between. The figure clearly shows that the results are very stable up to around $1.7\ m$. Thus, adding more wave cuts results in a more stable outcome, even for numerically calculated wave fields, where measurement error plays no role.

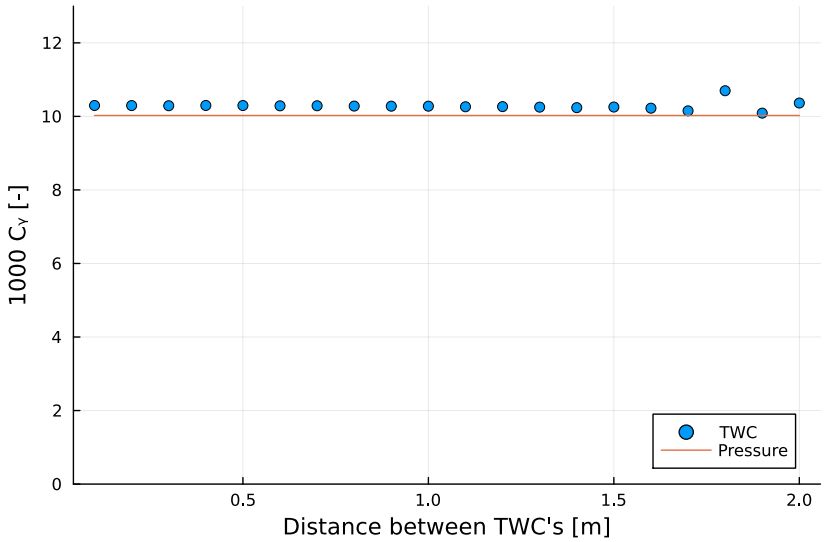

Figure 5.3: Side force plotted over the distance between first and last wave cut for 8 wave cuts

5.1.2. Width of TWC

The width of the transverse wave cut is a parameter that affects the calculation of the side force. First, the width must be large enough to capture the entire wave field. The wave field is confined within the Kelvin angle of 19.47°, so the minimum required width follows from the Kelvin angle multiplied by the distance to the last wave cut. For this case, it results in a width of 1.556 meters.

The width also directly influences the spacing between the discrete transverse wave numbers, since $u_n = \frac{\pi n}{b}$. A larger width reduces the spacing, resulting in a finer discretization of the wave spectrum.

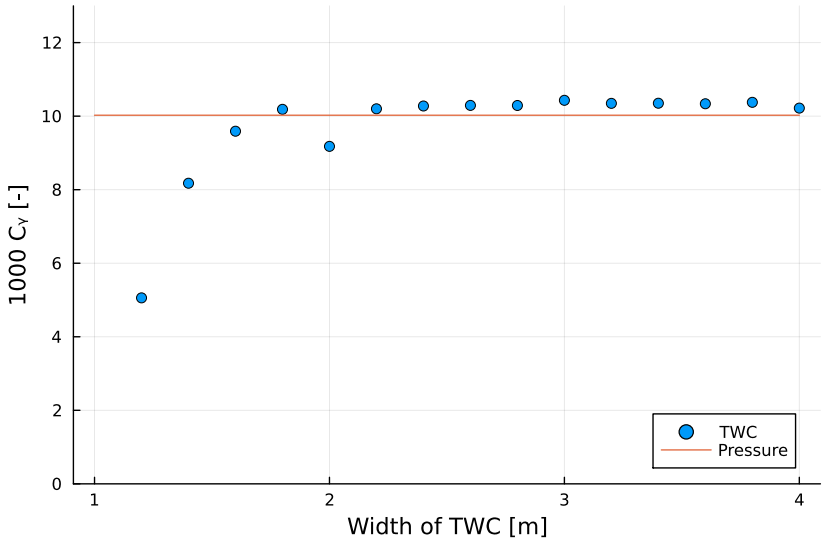

Figure 5.4: Side force plotted over the width of the TWC

The effect of varying width on the side force is shown in Figure 5.4. For widths below the minimum criterion, the results deviate significantly from the pressure integration. This is expected, since part of the wave field is not captured. At the exact minimum width, the results are still not fully converged because the waves at the Kelvin line are at their peak and have not yet decayed. A slightly larger width is therefore needed to allow the waves to fully dampen out before the cut is applied.

From approximately $b = 2.5$, the side force results are stable and show good agreement with the pressure integration, indicating sufficient convergence. It seems that the width of the wave cut does not influence the result much beyond this point. It can be concluded from this point that the spacing between the transverse wave numbers u_n does not matter much for the result. In this analysis, 80 wave numbers have been used for the determination of the coefficients. For the highest wave numbers, no contribution is found anymore, and the side force result is converged. If the spacing decreases too much, the higher modes fall outside the evaluated range, so more wave numbers would need to be included.

5.1.3. Wave spectrum

The wave spectrum consists of the contribution to the force for each wave number. The results for the resistance and the side force are shown in Figure 5.5. The spacing between the points is evenly spaced as u increases with $\frac{\pi}{b}$. Here, b is made non-dimensional with the basic wave number k, and therefore, u is also non-dimensional. The integral of the force component over the wave number is the total (non-dimensional) force on the hull.

The wave resistance distribution peaks at the lowest wave numbers. Low wave numbers correspond to transverse waves, i.e., the waves are traveling in the direction of the ship. This means that for this case, the transverse waves contribute the most to the wave resistance. The side force starts at zero and peaks at higher wave numbers. It is expected that purely transverse waves don't contribute to the side force. Both methods converge to zero for large wave numbers. The resistance force converges faster than the side force, meaning that the side force needs more wave components to converge.

For the resistance force, the first value at $u = 0$ is not the largest, whereas a purely transverse wave ($u = 0$) is expected to have the largest contribution to the wave resistance. This is a direct consequence of Neumann's factor $\epsilon_0 = \frac{1}{2}$. Without this factor, the first point would indeed be the highest, consistent with physical expectation.

The Neumann factor is purely a mathematical correction from the discretization of the force integral. The original integral runs from $-\infty$ to ∞ and is folded to 0 to ∞ by symmetry, such that each discrete mode $n \geq 1$ represents a full interval $\Delta u = \frac{\pi}{b}$ centered around u_n. For the first value $n = 0$, the mode, however, sits exactly on the boundary, and therefore only has half an interval on the positive side, giving it an effective width of $\frac{1}{2}\Delta u$. The factor $\epsilon_0 = \frac{1}{2}$ accounts for this. In the graph, the smaller value should therefore not be interpreted as a low contribution of the $u = 0$ wave, but simply that this mode only represents half of the integration domain compared to the other waves. The same is the case for the side force integral, but as the contribution of $u = 0$ is so small, no effect can be seen.

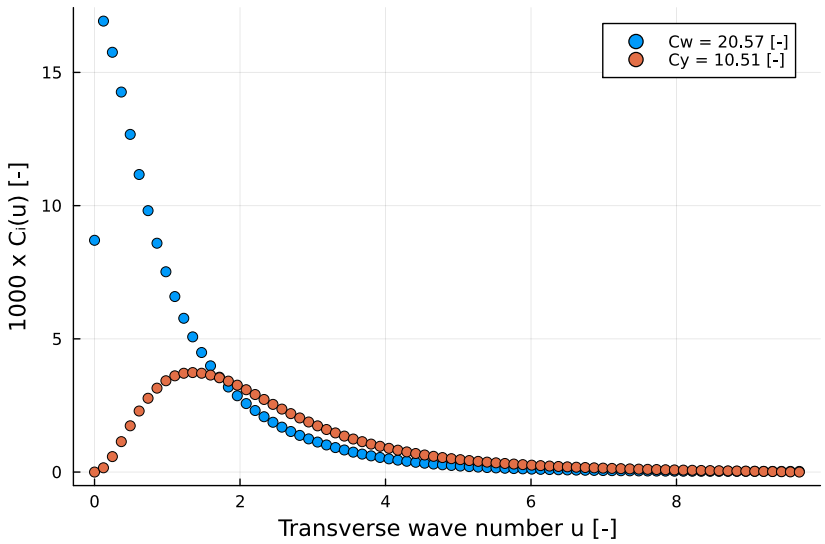

Figure 5.5: Side force wave spectrum using the transverse wave number u

By using the relation between the wave angle θ and the transverse wave number u, a similar figure can be created, which has more physical sense. In Figure 5.6, the y-axis shows the contribution to the force, but on the x-axis, the wave number has been changed for the wave angle. It is now possible to see the contribution of each angle in the decomposed wave field. The wave angle is given in degrees. The decomposition includes odd and even parts, so the angle for each wave could be negative or positive, thus propagating in the starboard or port side direction. The spacing between the points is not equal, as the transformation asymptotically converges to 90 degrees as the wave number increases. Therefore, the integral is not equal to the total force. Nevertheless, it can provide insight into the origin of the force.

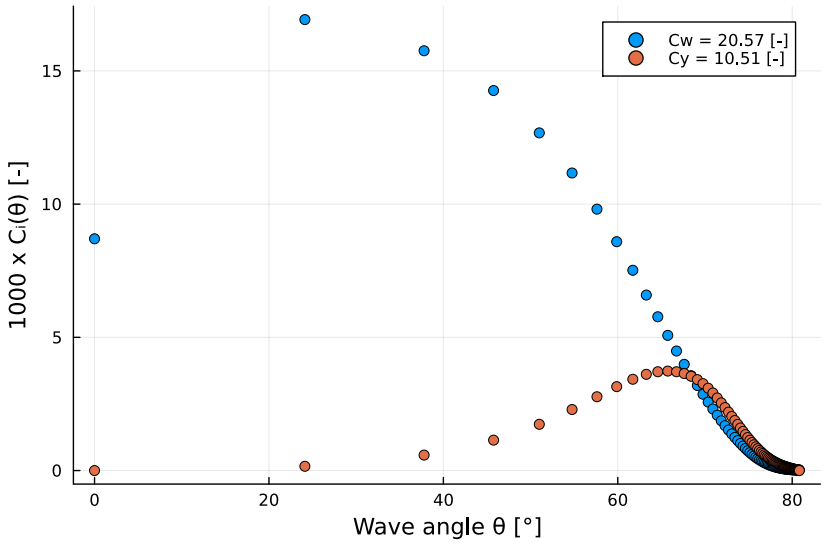

Figure 5.6: Side force wave spectrum using the wave angle θ

Here, the difference between the two force components is even more apparent. The peak of the wave resistance force is around 20 degrees, while the side force peak is at 65 degrees.

The spacing does not give ideal visualization for lower wave angles. This could be changed by calculating the force components for a uniformly distributed set of angles (β) rather than using the transverse wave number u. It would, however, require changing a large part of the method.

The general Kelvin wake pattern can be seen in Figure 5.7. The general wake consists of transverse and diverging waves. Right behind the ship, the waves travel in the same direction as the ship ($\theta = 0$). The wave angle increases further away from the midline. On the boundaries, the value of the transverse wave reaches a value of $35°$. Larger values of θ are considered diverging waves. At the Kelvin angle, the transverse and diverging waves meet with a common angle of $35°$.

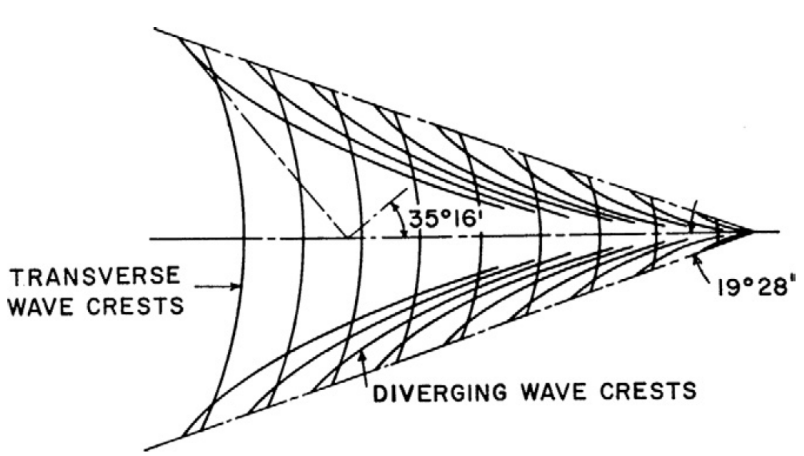

Figure 5.7: Kelvin-ship wave pattern (Newman, 2017 [21])

The side force formula from Sharma (1964) [24] was given as:

$$F_y = \frac{\pi}{2} \int_{-\frac{\pi}{2}}^{\frac{\pi}{2}} [f^2(\theta) + g^2(\theta)] \cos^2(\theta) \sin(\theta)\, d\theta \tag{5.1}$$

f and g are parameters defined by the wave pattern. These are then multiplied by the factor $\cos^2(\theta)\sin(\theta)$. This has been plotted, and the result can be seen in Figure 5.8. The peaks correspond to the same angles of $35°$.

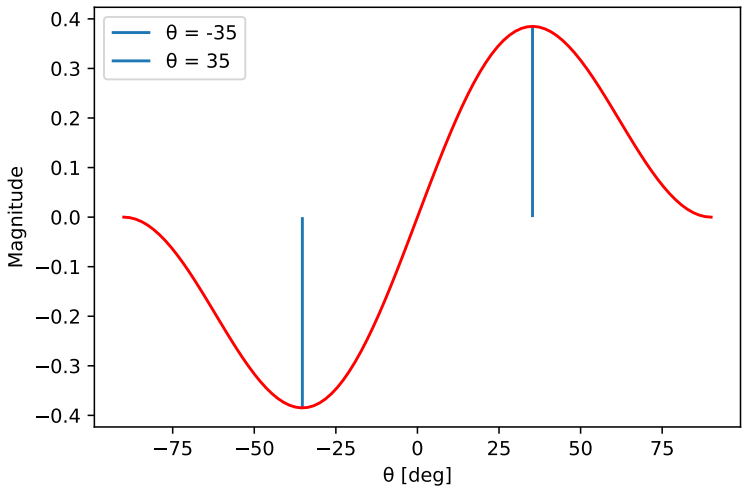

Figure 5.8: $\cos^2(\theta)\sin(\theta)$ plotted

In the wave spectrum plot, the largest contribution to the side force is around $65°$. This does not correspond to the (strongest) wave angle of $35°$, stated previously. It turns out that the largest contribution to the side force occurs at larger wave angles. As the peak exceeds $35°$, it can be concluded that divergent waves dominate the contribution to the side force.

For the resistance, this is not the case. Most contribution is given by the transverse wave numbers, but a little contribution is also made by diverging waves. While for the side force, almost all contributions were only from diverging waves.

A submerged spheroid has a relatively simple wave spectrum compared with ships. For ships, the wave pattern is more complex due to their geometry and the surface-piercing effects. For a ship, it can aid in design and give valuable insights into wave forces.

5.2. Ecoliner - RANSE

The Ecoliner has been tested in the numerical towing tank of OpenFOAM. Two versions of the simulation will be performed. The first case simulates the flow using the standard settings. The second iteration has changes to the settings to enhance the result of the wave pattern, aiming to be more suitable for a TWC analysis.

The vessel has been scaled $(1:50)$ and will be tested for a Froude number of $Fn = 0.210$ and a drift angle of $\beta = 3°$. The velocity and drift angle have been chosen because they are realistic operating conditions for the vessel. Four wave cuts are used, as it is found that the results are more stable than two wave cuts. The matrix method is therefore used to obtain a least squares solution to the overdetermined system. The distance between the cuts is set at 0.05 m, and 300 frequencies are included in the Fourier transform.

5.2.1. Version 1 simulation

The results of the simulation with no changes will be discussed in this section. The simulation has been performed as written in the methodology. The wave field can be extracted from the data. The result in Figure 5.9 shows the wave pattern of the Ecoliner. From the figure, the Kelvin wake refinement region can be identified. After some distance to the stern, the wave pattern suddenly disappears. Outside the refinement region, the cell size increases, which causes wave damping.

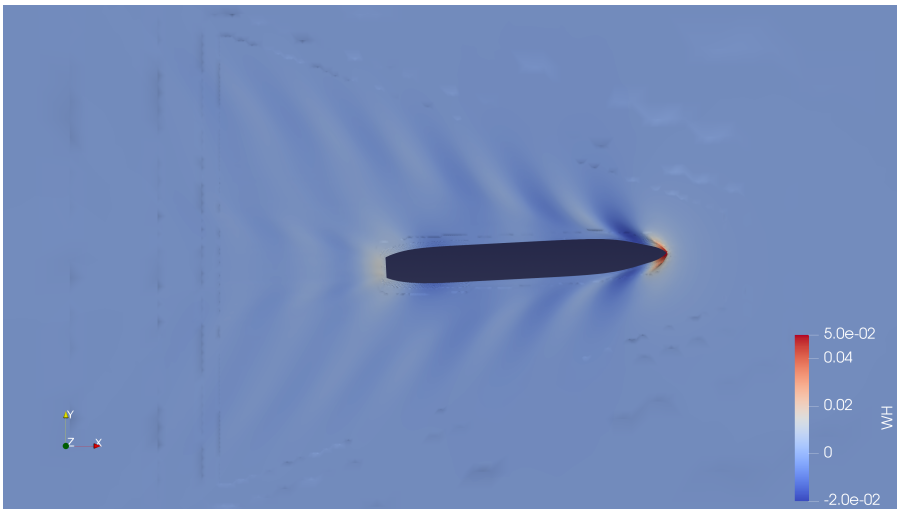

Figure 5.9: Wave pattern of the Ecoliner from version 1

The TWC method will be applied to the obtained wave pattern. The first sanity check is to verify that the TWC method returns the same outcome across different longitudinal locations. It is expected that the result varies very little across the location of the wave cut, which would indicate a successful implementation of the method. Exceptions are close to the hull and outside the Kelvin wake refinement region. Near the hull, near-field effects are present. Here, some deviations are expected, as the wave pattern cannot be reconstructed from a superposition of linear waves. Outside the Kelvin wake refinement region, the wave elevation is expected to decay rapidly. This will cause the wave-induced forces to decay. In the Figure 5.10, the result can be seen.

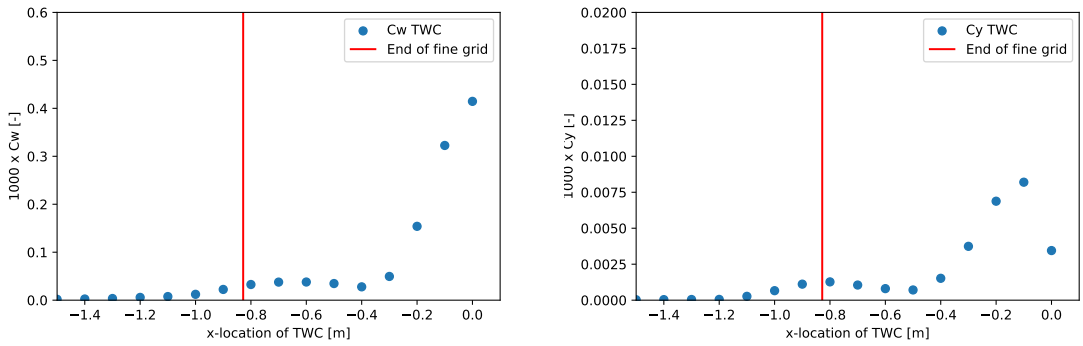

(a) Wave resistance

(b) Side force

Figure 5.10: Force for different longitudinal positions of the TWC

For the wave resistance, the three regions are clearly visible. First, the near-field region can be seen, showing the largest values for the wave-induced forces. The influence of the hull amplifies the flow in such a way that the assumptions of the linearized waves do not hold. The waves can be steep, which breaks the low steepness assumption, and the flow can be rotational. The quadratic terms in the derivations and the boundary conditions can therefore not be omitted.

This near-field region decays rapidly, and the wave resistance stabilizes slightly. Here, the wave pattern should be valid to apply the TWC, as it is inside the refinement region and outside the near-field affected area. For this simulation, this region is only 0.3 meters long. Further back outside the area, the fine grid region ends, and the wave resistance decays rapidly to zero. The side force also shows the same three regions. The big difference is that the force values are much lower than the resistance force. This is to be expected, as the ship has a small drift angle.

Extending the wake refinement region

The region where the forces can, in theory, be calculated correctly is very much dependent on the length of the Kelvin wake refinement. In this simulation, this region is very short, and a part cannot be used due to near-field effects. It is difficult to draw conclusions from this. To enlarge this region, the same simulation was run, except that the Kelvin wake refinement was extended to $0.6L_{pp}$. This should increase the suitable region by $0.83\ m$. The expansion of the wave cut has increased the number of cells to 2.1 million. The result of the TWC result can be seen in Figure 5.11.

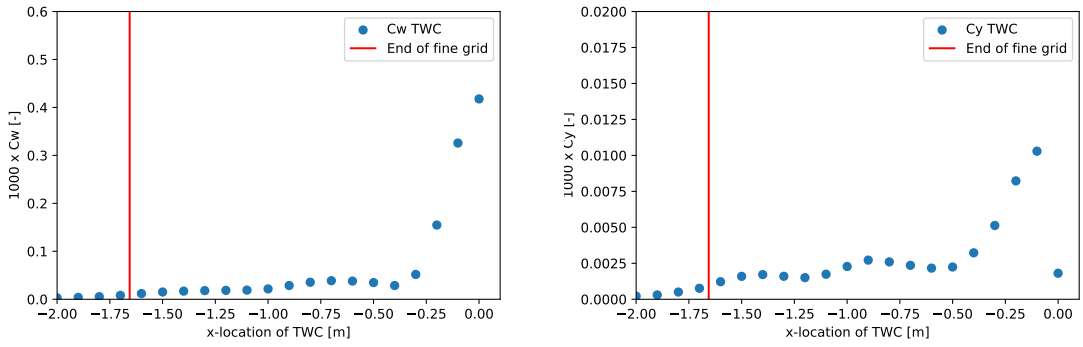

(a) Wave resistance

(b) Side force

Figure 5.11: Force for different longitudinal positions of the TWC

The results are quite similar to the previous version, except that the valid region where the TWC can be evaluated is larger. The forces show slower decay for a longer distance behind the hull. The extra length of the refinement region makes it possible to estimate the decay rate of the wave resistance. It

is expected that the wave resistance decays exponentially. An exponential curve is fitted to the data, and from this, the decay per wave length can be calculated. The curve will be fitted in the region where the wave cut method is considered valid, excluding the near-field effects and inside the fine mesh area. It is difficult to find the exact boundary where the near-field effects end. From the literature, it has been found that near-field effects are observed up to $0.3L_{pp} - 0.5L_{pp}$ [22]. The refined Kelvin wake has the length of $0.6L_{pp}$, so it has been chosen to consider the near field effects reduced from $0.3L_{pp}$. The curve will be fitted from $0.3L_{pp}$ till $0.6L_{pp}$. From the curve, it is possible to calculate the decay per fundamental wavelength $\lambda = \frac{2\pi}{k_0}$.

The fitted exponent can be seen in Figure 5.12. It has been zoomed in on the region of interest, omitting the near-field affected region. The region between has been marked with the red lines, and the number of wave cuts and the distance between the wave cuts have been taken into account, so that when the calculations are made, all wave cuts fall within this region. The y-axis has been showing a log scale, so that it is possible to view the x and y forces in the same plot and compare them directly. On a log scale, exponential decay appears as a linear slope.

Both the wave resistance and side force decay in an oscillatory manner. Both follow roughly the same path, but the wave resistance is 10 times larger. The wave resistance decays with a rate of $51.7\ \%$ per wave. The rate is similar for the side force, as this force decays with $48.0\ \%$. This is expected, as both of the wave-induced forces scale with the wave elevation squared, $F_w \propto \zeta^2$.

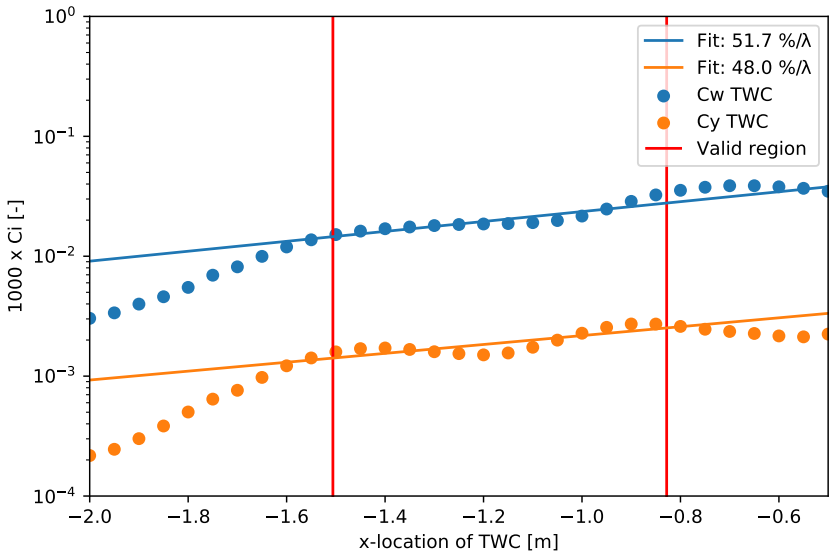

Figure 5.12: Exponential fit for the decay of the wave forces

The decay for the wave-induced forces is very large for this CFD simulation. A real wave pattern would show some decay due to the friction in the water. However, this is usually very low and would not cause it to dampen out more than $50\ \%$ in a single wave. It is likely that only the stern wave has a contribution, as the bow wave has damped out almost completely.

It can be concluded that the wave pattern behind the ship is not accurately represented by the CFD simulation. The effect of numerical damping is large and unrealistic. In this case, the TWC method was not really used to calculate the wave resistance due to the errors in the simulation. However, it still gave insight into the effect of the mesh and the quality of the simulation.

5.2.2. Version 2 simulation

A second iteration of the simulation has been conducted to improve the wave pattern behind the hull. This method uses the Euler time scheme instead of the localEuler time scheme. For the first simulation,

this is the only difference. After the result has been reviewed, different refinement levels for the Kelvin wake region are tested. The duration of the simulation was much longer. Version 1 took about 2 hours for the full simulation, while this version took about 18 hours. It is expected that this will result in a more accurate wake simulation.

Evaluation of TWC-location

The resulting wave field from the second iteration can be seen in Figure 5.13. The wave field shows more color than the first simulation, especially near the boundary for the Kelvin angle, meaning that the wave shows less decay.

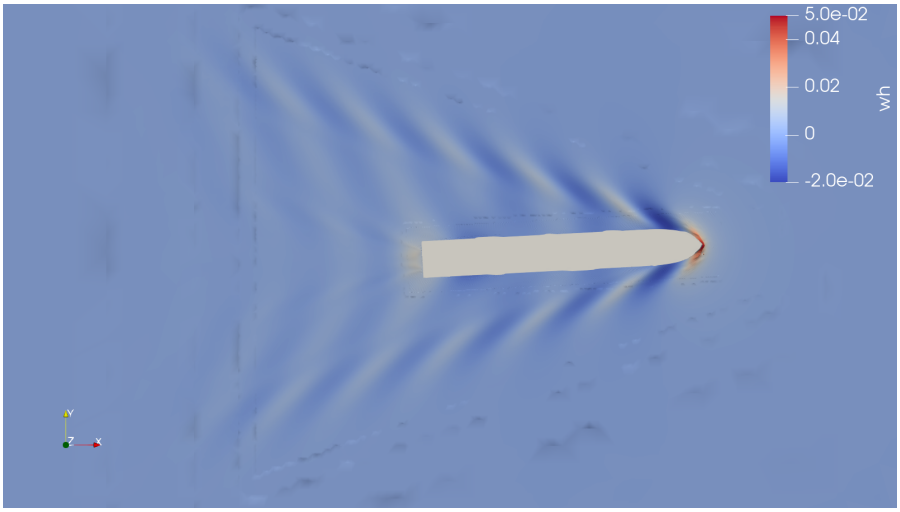

Figure 5.13: Wave pattern of the Ecoliner from version 2

The same plot as shown in Figure 5.12 can be made for this simulation, to check if the damping is indeed less than the first version. Again, an exponential fit has been fitted to the two forces, and the decay rate per wave has been calculated. The result can be seen in Figure 5.14.

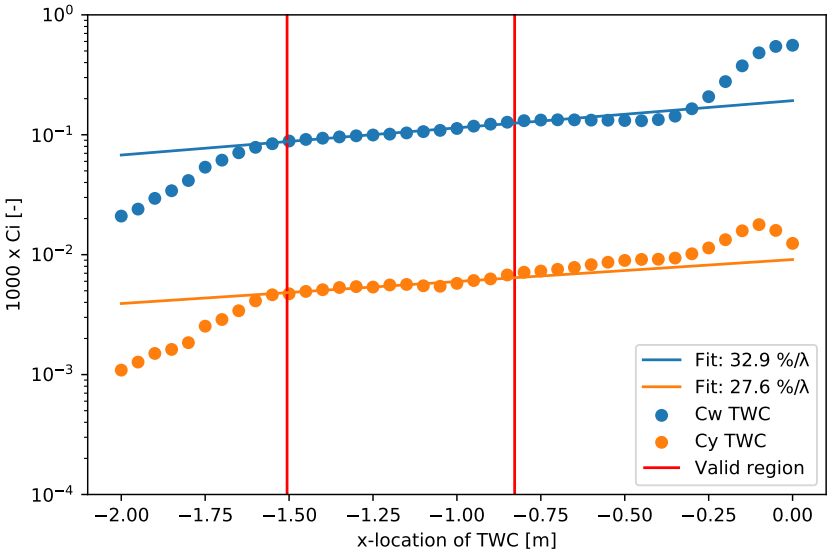

Figure 5.14: Exponential fit for the decay of the wave forces

The forces show similar behavior. It can be seen that the slope of the decay is less steep, and this is

confirmed by the calculated decay rate. The decay for the resistance and side force are respectively, $32.9\ \%$ and $27.6\ \%$. The biggest difference is that both forces are overall almost ten times larger than in the previous version. The wave pattern consists of contributions from the stern and the bow of the vessel. The stern wave travels only a short distance to reach the measurement location and is therefore less affected by numerical damping. The bow waves travel a considerably longer distance along the hull before reaching the TWC location. This would make the bow wave more susceptible to numerical damping. It is likely that the representation of the bow wave has had the biggest improvement with this simulation, which would explain the significant increase in the predicted forces.

It is interesting to see that changing the time scheme leads to a significant improvement in the quality of the simulation. It turns out that for far-field effects, the localEuler time scheme is not the appropriate method.

Mesh refinement effects

For version 2, different refinement regions have been simulated. By varying the mesh of the Kelvin wake refinement region, it can be investigated how large the effect on wave damping is. The results shown have a refinement value of 5. Two additional simulations will be performed with refinement values of 4 and 6. An increase or decrease of 1 level will result in a cell size that is twice as large or small as the original mesh size. For the simulation with refinement level 6, it was not possible to expand the mesh refinement region to $0.6L_{pp}$. The number of cells turned out to be too large because the supercomputer's runtime limit was exceeded. Therefore, the end of the refinement region was set to $0.5L_{pp}$. This reduced the number of cells just enough to run the simulation. The result of the simulation for the different refinement regions can be seen in Figure 5.15.

Overall, the wave resistance increases with higher refinement. The distance between the refinement levels 5 and 6 is still quite big. The decay level decreases with each refinement level, consistent with expectations. The highest refinement level shows a 3.3% decay. This is already quite low. However, as the distance between refinement levels remains significant, it cannot be concluded that the results are near convergence.

The length of the near field region (the peak near the ship) stays the same for different refinement regions. This suggests that the boundary could be moved slightly toward the ship to enlarge the valid region. The wave resistance shows a less oscillatory behavior at higher refinement levels, which would also indicate a more accurately simulated wave field.

For the side force, the oscillatory behavior is larger for a higher refinement. The highest refinement shows a negative decay rate, suggesting that the wave elevation increases. For this refinement, the region is up to $0.5L_{pp} = 1.38\ m$. Therefore, the valid region for the exponential curve fitting is rather small. The force has an oscillatory behavior, and the region contains only half a wavelength, which causes inaccuracies in the result of the decay. Shifting the near-field boundary more to the stern would reduce the error. The other mesh refinement plots also produce ambiguous fitting results. The lowest mesh shows results below zero and shows a slow decay of 4.4%, while the highest decay rate would be expected. The results from the fitting process can not be deemed reliable due to the wavy and unexpected decay rate.

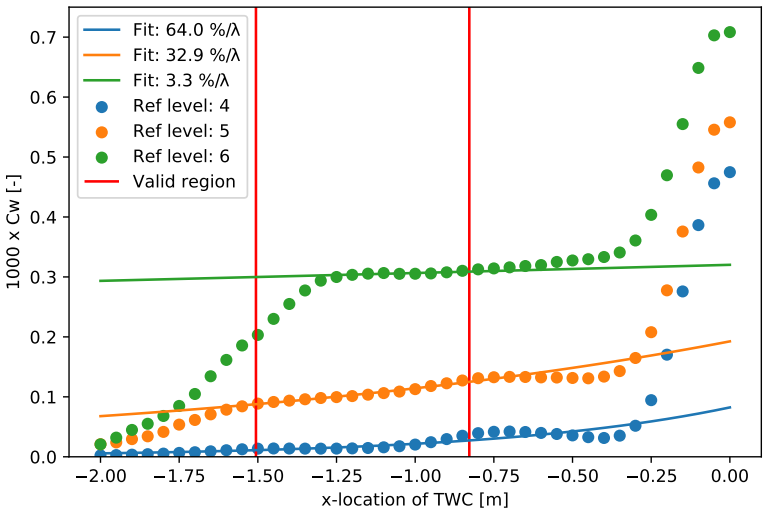

(a) Wave resistance decay for different refinement levels

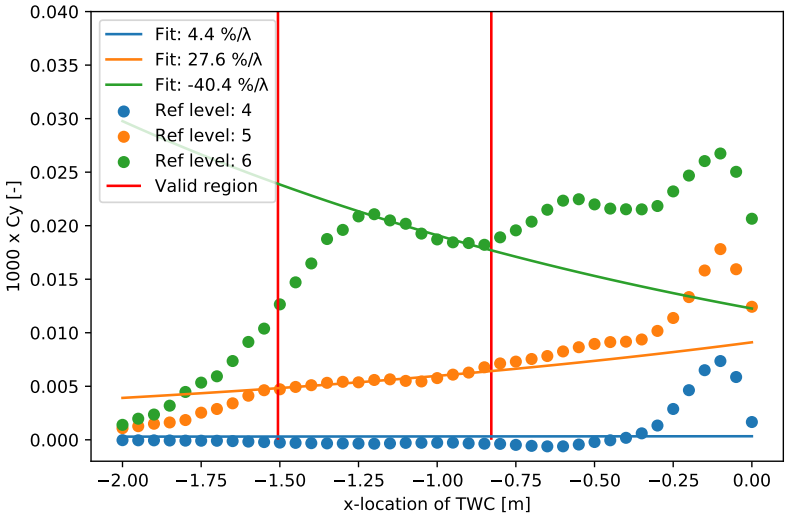

(b) Side force decay for different refinement levels

Figure 5.15: Exponential fit for the decay of the wave forces

The wave resistance yields results more in line with expectations, whereas the side force shows oscillations and a negative value. To further investigate the cause of this, some information can be taken from the previous wave spectrum analysis. From this, it was found that wave resistance is primarily caused by transverse waves. For the side force, diverging waves are dominant. For the submerged spheroid, the dominant waves were at around $65°$. It is possible to write the wavelength as a function of the wave angle relative to the ship:

$$\lambda(\theta) = \frac{2\pi U^2}{g} \cos^2(\theta) \tag{5.2}$$

This relation shows that the wavelength is smaller for diverging waves. A finer mesh is required to accurately describe waves with a shorter wavelength. For the submerged spheroid, waves with an angle of $65°$ showed the most contribution to the side force. A quick calculation can give the wavelength

relative to the wavelength of purely transverse waves. $\cos^2(65°) \approx 0.18$, therefore, the wavelength is only about 18% to that of purely transverse waves. To maintain the same resolution for the diverging waves, the mesh should be increased by a similar factor. In practice, this would require an additional level of refinement, which is not feasible within the current computational constraints. This could be one of the reasons why the side force shows a highly oscillatory result for the highest grid refinement.

The mesh of the simulation is mostly built with hexahedral cells, aligned with the undisturbed flow direction. From the literature, it was found that the mesh should be aligned with the flow to reduce numerical damping. For transverse waves, contributing to the resistance force, the cells in the simulation are in line with the flow direction. For diverging waves, contributing the most to the side force, the cells are not aligned with the direction of the flow. This causes the waves to cross cell faces diagonally, increasing the numerical dissipation.

The wave resistance is calculated from the total wave energy in the transverse wave cut. Each individual wave's contribution has a positive effect on the force, regardless of direction or magnitude. The side force, however, depends on the difference between the waves traveling port and the waves traveling to the starboard. For small drift angles, the magnitude of these contributions can be close to each other. The side force is essentially the (small) difference between the contributions. Therefore, small errors in the wave elevation can have a large effect on the computed side force. This would be the reason that computing the side force is, in essence, more sensitive to errors than the wave resistance.

These three factors combined can explain why the wave resistance is predicted more reliably than the side force. The transverse waves dominating the wave resistance have a longer wavelength, are better resolved on the current mesh, and propagate in line with the cell alignment. The diverging waves dominating the side force are shorter, cross the mesh diagonally, and their contribution depends on the small difference between port and starboard components, making it more sensitive to numerical errors.

Wave investigation

To investigate further into these results, a step back can be taken, and the wave pattern can be investigated. For this, two wave cuts have been made, and the results have been plotted. Both cuts can be seen in Figure 5.16. The first wave cut is along the x-axis. With this, the wave elevation right behind the ship can be seen. The second cut follows the Kelvin angle, starting at the bow wave. This shows the wave propagation over a much longer domain.

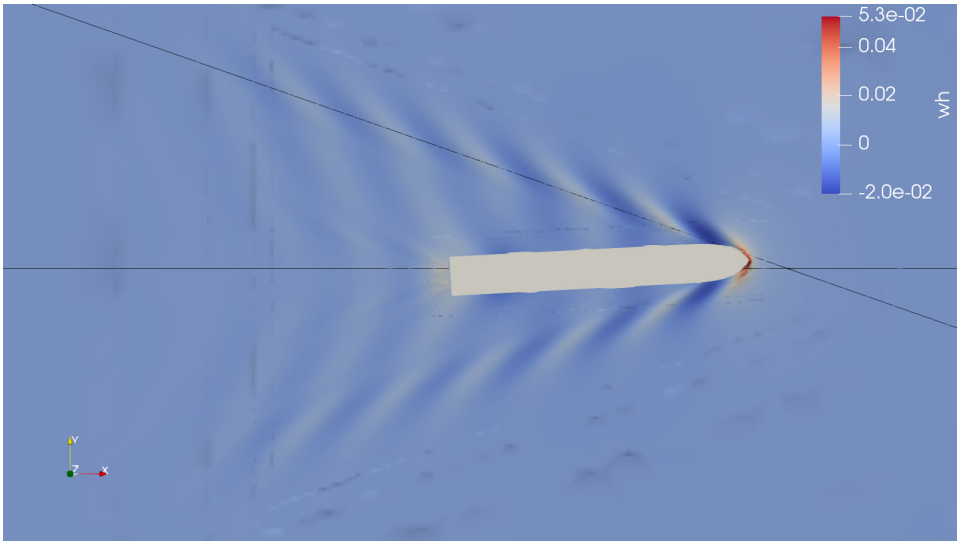

Figure 5.16: Wave cut location

In Figure 5.17a, the wave elevation along the x-axis right behind the ship can be seen. The highest peak is located near the stern, where the hull ends and the stern wave is generated. After this peak, the wave elevation decreases as the wave propagates downstream. This peak explains why the wave-induced forces show higher values in the near-field region close to the stern. The wave elevation is very

similar for the three different refinement regions. The similarity between refinement levels suggests that this region is less sensitive to mesh resolution.

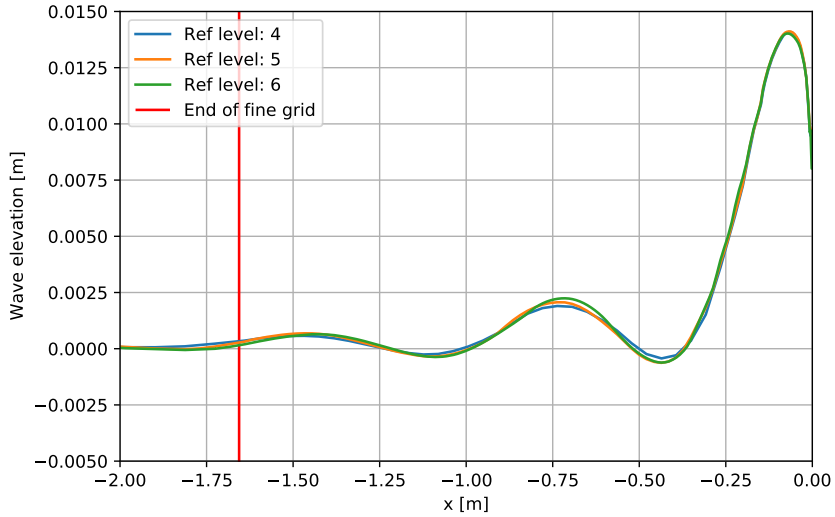

(a) Longitudinal wave cut behind the stern

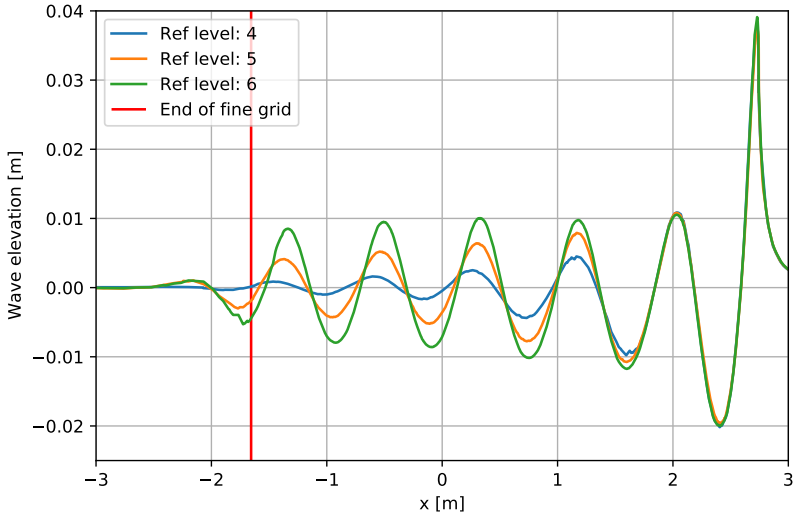

(b) Wave cut following the Kelvin angle

Figure 5.17: Wave cuts for different refinement levels

The wave elevation along the Kelvin angle is shown in Figure 5.17b. A peak can be seen at the bow wave, where the wave elevation rises sharply. Moving away from the bow, the wave elevation decays at a rate that is strongly dependent on the mesh refinement level. At the lowest refinement level, the wave has almost completely damped out before reaching the wave cut evaluation location. At the highest refinement level, the wave amplitude is preserved significantly better over the same distance, demonstrating that the mesh can resolve and propagate the wave with much less numerical diffusion. This clearly shows the strong influence of mesh refinement on numerical wave damping.

The Kelvin wave cut is much more affected by numerical damping than the longitudinal cut behind the stern. At the lowest refinement level, the wave has almost fully damped out before reaching the TWC measurement location. The stern wave is much less affected by the refinement level. The reason for

this is most likely because the wave has to travel less far to reach the TWC. The wave passes through fewer cells, and since each cell contributes a small amount of numerical diffusion, the cumulative effect is much smaller over this shorter distance.

To make a quantitative analysis of the decay of the wave, again, an exponential function can be fitted to the wave pattern. The wave is approximated by a sine function with an exponential decay. A function can be written as:

$$f(x) = ae^{-bx} \sin(\omega x + \varepsilon) \tag{5.3}$$

The analytical function was fitted to the wave pattern in the refined mesh region, excluding the area close to the bow where strong nonlinear effects may introduce inconsistencies. Through this fitting procedure, the coefficients of the function were determined. Using the exponential decay coefficient (b) and the angular frequency (ω), the decay rate per wavelength can be evaluated as:

$$\text{Decay per wavelength} = 1 - e^{\frac{2\pi}{\omega} b} \tag{5.4}$$

In Figure 5.18, the fitted function is plotted over the Kelvin angle wave. It can be seen that the curve follows the wave accurately. The bounds of the fitting process can also be seen. The fit begins on the second wave after the bow wave peak, and ends when the fine mesh ends. Here, the result for the simulation with refinement level 5 is shown. A similar analysis has been performed for the other refinement levels. These results of the decay rate per wavelength can be seen in Table 5.1. The fitting process for the longitudinal wave behind the stern was not performed because it proved unreliable due to the very short domain.

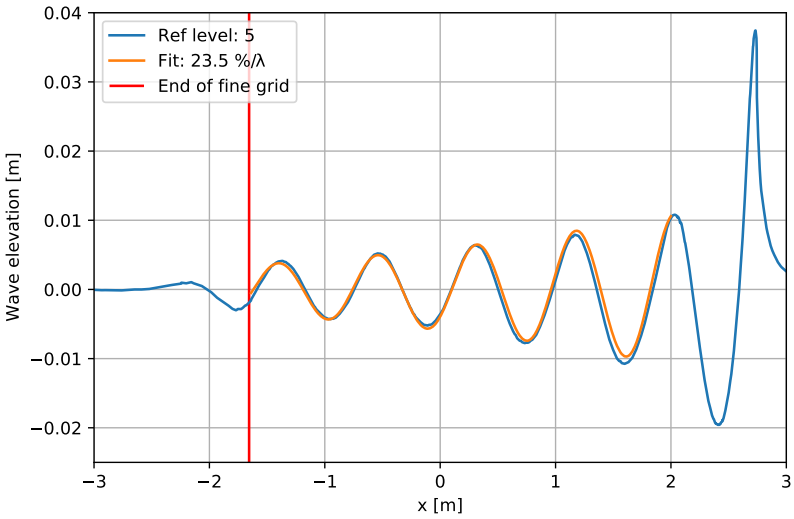

Figure 5.18: Function fitted to the Kelvin wave

Refinement level	Decay wave per wave length [%]	Decay of TWC per wave length [%]
4	57.0	64.0
5	23.5	32.9
6	7.5	3.3

Table 5.1: Decay for different refinement levels

The results show a strong reduction in decay rate with increasing refinement level, dropping from 57.0% per wavelength at refinement level 4 to 7.5% at refinement level 6. This confirms that mesh refinement has a significant effect on numerical wave damping.

The third column shows the corresponding decay rates obtained from the wave resistance calculated by the transverse wave cut method. These differences in the decay rate may be attributed to the fact that the two methods measure different aspects of the wave field. The Kelvin cut follows the wave along a specific angle, while the transverse wave cut integrates the full wave pattern across the entire wave field.

5.2.3. Assessment of simulation quality

In this study, the TWC method could not be used reliably to calculate the wave forces due to the poor quality of the CFD simulation. It was found that the mesh refinement in the Kelvin wake should be very fine and should be enlarged for the TWC method. Outside the refinement region and close to the hull are areas where the TWC method is not valid. Increasing mesh refinement improved the quality of the simulation.

While the TWC method did not give the intended results, it still provided valuable insight into the effect of mesh resolution and the quality of the simulated wave pattern. By extracting the decay rate from the transverse wave cut, the method was used to quantitatively assess numerical dissipation in the CFD method. The method can therefore serve a dual purpose. Beyond its intended use as a wave-induced force calculation method, it can also be used as a diagnostic tool to assess the quality of the simulation.

6

Conclusion

In this research, the goal was to answer the main research question:

> *To what extent can side forces acting on a ship be accurately determined from a calculated wave field using the transverse wave cut method?*

The main question has been split into sub-questions to help answer it. They will be answered based on the simulation results. After this, the main question will be answered.

6.1. Fourier transform

How can a Fourier transform of the transverse wave cut be used to obtain the side force?

The side force approach follows the same procedure as used for the calculation of wave resistance. The only difference is in the final formulation of the force. The formula for the side force was given by Sharma [24]. However, this approach has not been tested before, thereby defining the research gap. To be consistent with the wave resistance method, the equation was rewritten from the angular domain (θ) to the transverse wave number domain (u). Once this transformation was performed, the same Fourier coefficients could be used. As a result, most of the methodology remains unchanged, as only the final force expression differs. When using wave pattern analysis from a TWC, the wave-induced side force can be directly obtained with no extra effort.

6.2. Varying conditions

How does the side force obtained from the transverse wave cut method compare to that obtained from pressure integration under varying location, angle, speed, and grid size?

For the simple case of a submerged spheroid simulated with a panel method, the results are close to the results from the validated pressure integration. For different yaw angles and speeds, the wave cut method produced results that were almost similar. For different longitudinal wave cut locations, the results remain constant and correspond with pressure integration. Only very close to the hull, an expected deviation was noticed, caused by near-field effects. A grid resolution study also showed that the wave pattern converges to the same value as the pressure integration. All these results demonstrate that the method is valid.

6.3. Wave spectrum analysis

What insights can wave spectrum analysis provide for side forces?

Wave spectrum analysis uses the same coefficients as the transverse wave cut formulation, so it does not add computational time. For each transverse wave number, the contribution to the relevant force can be examined. Even more insight can be gained by converting the wave number to the wave angle. Now the contribution to the wave force can be visualized for different wave angles, giving insight into

the causes of wave-induced forces.

For wave resistance, the analysis showed that the main contribution comes from transverse waves, while diverging waves contribute little. In contrast, only diverging waves contribute to the side force. The largest contribution occurs at approximately 65 degrees, which is higher than the angle at which transverse and diverging waves intersect along the Kelvin wake pattern.

6.4. CFD simulations

To what extent can the transverse wave cut method be used in CFD simulations?

The quality of the wave pattern simulation depends on the mesh size. Wave damping increases for coarser meshes, leading to a faster decay of the wave field. From transverse wave cuts performed at different longitudinal evaluation locations, it was shown that the calculated force is not constant for the CFD OpenFOAM simulations. An exponential fit was applied to determine the decay rate per wavelength. It was shown that the decay rate was reduced by using the Euler time integration scheme and refining the Kelvin wake region. Although this increased the wave forces, a converging pattern was not yet recognized for the different mesh refinements.

The results for the wave resistance are stable, in line with the expectations, while the side force showed more oscillating behavior, with less accurate results for the decay rate. The side force is more sensitive to numerical errors than the wave resistance due to the shorter wavelength of diverging waves, their diagonal propagation relative to the mesh, and the fact that the side force depends on the small difference between port and starboard wave contributions.

The TWC method did not provide the intended force results. However, it still provided insight into the effect of mesh resolution on the quality of the simulation of the wave pattern. Using the decay rate from the TWC method, a quantitative assessment of the numerical damping of the CFD method can be made. The method can serve a second purpose: evaluating the quality of the CFD simulation.

6.5. Main question

To what extent can side forces acting on a ship be accurately determined from a calculated wave field using the transverse wave cut method?

The transverse wave cut method can provide accurate estimates of wave-induced side forces from a calculated wave field. It shows good agreement with pressure integration when the wave pattern is accurately simulated by a panel method, but its accuracy is limited by mesh resolution and numerical dissipation in CFD simulations.

7

Recommendations

From the results of this research, the following recommendation can be made for further research:

- **Shallow water effects:** Infinite depth was assumed for all derivations and calculations in this research. For deep water, the single wave potential is scaled with e^{kz} for the depth z. If finite depth is assumed, this factor changes to $\frac{\cosh(k(h+z))}{\cosh(kz)}$, where h is the water depth. This changes the final formula, which calculates the force from the Fourier coefficients. For wave resistance, it has been shown that the force can be calculated from wave pattern analysis in shallow water. It is expected that it is also feasible for predicting the side force. Shallow water effects are, for example, relevant for ships operating in harbors. In these locations, ships often need to make maneuvers, causing the ships to operate at a drift angle. This induces a side force, which can be estimated using a transverse wave cut.
- **Circulation:** In some cases, lift is generated due to circulation. For a ship, this effect is generally quite low, but for a foil, this effect can be large. A lifting body (such as a foil) generates a vortex system. This contributes to the total pressure field and the wave elevation. The deformation caused by circulation effects may have a different character from that which the TWC method is designed to capture. The effect of this could be investigated further in research by testing a surface-piercing foil.
- **CFD package:** For this thesis, only OpenFOAM was available for CFD simulations. However, the results did not accurately describe the wave pattern. Excessive wave damping caused the TWC results to be incorrect. It would be worthwhile to investigate whether the results from industry-level CFD packages are more accurate and if they enable the use of the TWC method to determine the wave-induced forces.
- **Experimental results:** The TWC method could also be used for experimental results. When wave pattern analysis was first introduced, it was intended for wave fields obtained from experiments. Special attention is needed for measuring the wave elevation, which can be done using optical methods or with wave probes. This influences the number of data points, which in turn affects the number of Fourier coefficients. Each approach also introduces its own measurement errors. Additionally, reflection of the waves on the tank walls should also be taken into consideration, as this affects the placement of the TWC. It will be interesting to see whether the method correctly calculates the wave-induced forces for towing tank results.
- **Longitudinal wave cut method:** For the experiments, it might also be worth investigating the longitudinal wave cut method, because wave elevation data can be measured more easily for a longitudinal wave cut (LWC) than the TWC. A fixed probe can be placed in the water, measuring the wave elevation as the ship passes by. For the side force, at least one measurement is required on each side of the hull, since the side force is effectively obtained from the difference between the wave pattern to port and starboard. The wave pattern aft of the ship decays very slowly, so an asymptotic extension must be fitted to the end of the signal. In practice, finite measurement boundaries may pose challenges to accurately capture the side force.

- θ **equally spaced:** Interesting results were obtained from the wave spectrum plots. For different wave angles (θ), it was possible to see the contribution to the total wave force. The angle was obtained from the transverse wavenumber, which caused the wave angles to be unequally spaced. This resulted in low resolution at low wave angles and very high resolution at high wave angles. In this report, the transverse wave number (u) was uniformly spaced, and with that, the Fourier coefficients were calculated. Future research could calculate the Fourier coefficients with uniformly spaced wave angles. The effect on the calculation of the forces is unknown, but for the wave spectrum, it could increase resolution at lower wave angles.
- **Integral form result of TWC:** The TWC method originates from an integral equation over the plane behind the ship. The results for the wave resistance were consistent with the pressure integration results. For the side force, the results turned out to be different than the pressure integration. It has not been found out why this is the case. Future research could investigate this error.
- **Surface piercing ship in panel method:** The submerged spheroid was the only test case for the panel method in this research. This was chosen because an analytical solution exists for this case, which could be used for direct validation. Another reason was that the Neumann-Kelvin panel method was not suited for accurately simulating surface-piercing bodies. A logical next step is to simulate a surface-piercing hull using an appropriate panel method, such as a non-linear Rankine-based panel method. The pressure integration method is expected to be less accurate than for the submerged spheroid case, since the pressure distribution near the free surface intersection is more sensitive to the panel distribution. For the submerged spheroid, the convergence rate of the TWC method and pressure integration was similar. For a surface-piercing body, however, the TWC method is expected to converge more quickly. It will therefore be worthwhile to investigate whether the method is applicable to surface-piercing hulls, since it was originally developed for ships.
- **Extend method to also calculate moments:** In this study, the TWC method was extended to calculate both resistance and side force. It would be worth investigating whether it is also possible to calculate the moments acting on the ship from the far-field wave pattern analysis. For this, an angular momentum analysis must be performed. If successful, this would further extend the capability of the transverse wave cut method beyond forces alone.
- **Added resistance:** For this analysis, only ships sailing in undisturbed water were considered. In reality, ships sail in waves, which introduces additional forces on the ship. A calm water resistance prediction is therefore only part of the total resistance under realistic conditions. Extending the analysis of the TWC method to include incoming waves could be the next step. The incoming wave pattern must be known, and the simulation will become unsteady. The incoming wave pattern reflects off the ship, and the reflection causes a mean force. The extra force due to the waves is known as added resistance. For stationary structures, these forces are called the second-order drift forces. Even though the waves are oscillatory, a non-zero time-averaged force is present.

  Pressure integration calculates this effect on the hull by also integrating the second-order terms of the Bernoulli equation up to the water surface. For the wave cut method, it is not as straightforward. The wave gets reflected, and that reflection causes a force. To capture this, the undisturbed incoming wave field must be filtered out from the total wave pattern, leaving only the ship-induced modification. What remains contains the momentum flux corresponding to the wave forces.

  Since the second-order forces scale with $F^{(2)} \propto \zeta^2$, they are usually small and require accurate wave elevation predictions to extract reliably. Combined with the higher computational cost of unsteady simulations, this is left as a recommendation for future work.

References

[1] Pat Couser, J. Wellicome, and A.F. Molland. “An improved method for the theoretical prediction of the wave resistance of transom-stern hulls using a slender body approach”. In: 45 (Jan. 1999).

[2] K Eggers. “Basic Theory of Wave Analysis”. en. In: *Schriftenreihe Schiffbau* (1975).

[3] K Eggers. “On the determination of the wave resistance of a ship model by an analysis of its wave system”. In: *International seminar on theoretical waveresistance* (1964). URL: https://apps.dtic.mil/sti/citations/AD0615643.

[4] K Eggers. “Über die Ermittlung des Wellenwiderstandes eines Schiffsmodells durch Analyse seines Wellensystems”. de. In: *Schriftenreihe Schiffbau* (1962).

[5] K.W.H. Eggers, S.D. Sharma, and L.W. Ward. “An assessment of some experimental methods for determining the wavemaking characteristics of a ship form”. In: *Schriftenreihe Schiffbau* (1967).

[6] César Farell. “On the Wave Resistance of a Submerged Spheroid”. In: *Journal of Ship Research* 17.01 (Mar. 1973), pp. 1–11. ISSN: 0022-4502. DOI: 10.5957/jsr.1973.17.1.1. URL: https://doi.org/10.5957/jsr.1973.17.1.1 (visited on 03/26/2026).

[7] Thomas Henry Havelock. “The calculation of wave resistance”. In: *Proceedings of the Royal Society of London. Series A, Containing Papers of a Mathematical and Physical Character* 144.853 (1934), pp. 514–521. DOI: 10.1098/rspa.1934.0065. URL: https://royalsocietypublishing.org/doi/10.1098/rspa.1934.0065 (visited on 09/29/2025).

[8] Thomas Henry Havelock. “Wave resistance”. In: *Proceedings of the Royal Society of London. Series A, Containing Papers of a Mathematical and Physical Character* 118.779 (1927), pp. 24–33. DOI: 10.1098/rspa.1928.0033. URL: https://royalsocietypublishing.org/doi/10.1098/rspa.1928.0033 (visited on 09/29/2025).

[9] Justus Heimann. “Application of wave pattern analysis in a CFD based hull design process”. In: *Int. Numerical Towing Tank Symp. Tjärnö, Sweden.* 3rd (2000).

[10] Justus Heimann. “CFD based optimization of the wave-making characteristics of ship hulls”. English. In: (July 2005). URL: https://depositonce.tu-berlin.de/items/urn:nbn:de:kobv:83-opus-10442 (visited on 10/01/2025).

[11] J. Holtrop and G.G.J. Mennen. “An approximate power prediction method”. EN. In: *International Shipbuilding Progress* 29.335 (July 1982), pp. 166–170. ISSN: 0020-868X. DOI: 10.3233/ISP-1982-2933501. URL: https://journals.sagepub.com/action/showAbstract (visited on 10/02/2025).

[12] ITTC. *Practical Guidelines for Ship CFD Applications*. 2024.

[13] ITTC. *Wave Profile Measurement and Wave Pattern Resistance Analysis*. Recommended Procedures and Guidelines. 2021. URL: https://www.ittc.info/media/9605/75-02-02-04.pdf.

[14] Gunnar Jacobi. *Personal communication*. 2026.

[15] Joseph Katz and Allen Plotkin. *Low-speed Aerodynamics: From Wing Theory to Panel*. 1991. ISBN: 0-07-100876-4.

[16] N.J. van der Kolk. “Sailing Efficiency and Course Keeping Ability of Wind Assisted Ships”. en. PhD thesis. Delft University of Technology, 2020. DOI: 10.4233/UUID:8707309F-B9A3-4E09-916D-8FB64328A138. URL: http://resolver.tudelft.nl/uuid:8707309f-b9a3-4e09-916d-8fb64328a138 (visited on 03/04/2026).

[17] Anja Kömpe. *Implementation and Validation of a Wave Cut Analysis Method for the Wave Resistance Prediction from Potential Flow*. 2015. URL: https://www.semanticscholar.org/paper/Implementation-and-Validation-of-a-Wave-Cut-Method-K%C3%B6mpe/9cb4449bc5f4e13514f6ee04f52d8fa3422e3c54 (visited on 09/29/2025).

[18] Lars Larsson and Hoyte C. Raven. *Ship resistance and flow*. English. Principles of naval architecture. Jersey City, N.J: Society of Naval Architects and Marine Engineers, 2010. ISBN: 978-1-61344-138-1 978-0-939773-76-3.

[19] Toshiaki Mizuno and John V. Wehausen. “Determination of a Ship’s Wave Resistance in a Canal From Measurements of Wave Profiles”. en. In: (Dec. 1966). Number: HEL124. URL: https://apps.dtic.mil/sti/html/tr/AD0646729/index.html (visited on 11/04/2025).

[20] Anthony F. Molland, Stephen R. Turnock, and Dominic A. Hudson. *Ship Resistance and Propulsion: Practical Estimation of Propulsive Power*. Cambridge: Cambridge University Press, 2011. ISBN: 978-0-511-97411-3. DOI: 10.1017/CBO9780511974113. URL: https://www.cambridge.org/core/books/ship-resistance-and-propulsion/9BAA3B1283F70D4BA087DB0A64070419 (visited on 09/29/2025).

[21] J N Newman. *Marine Hydrodynamics*. 2017.

[22] Hoyte C. Raven and Henk J. Prins. “Wave pattern analysis applied to nonlinear ship wave calculations”. In: 13th (1998).

[23] S D Sharma. “A Comparison of the Calculated and Measured Free-Wave Spectrum of an Inuid in Steady Motion”. en. In: (1963).

[24] S.D. Sharma. *Untersuchungen über den Zähigkeitsund Wellenwiderstand mit besonderer Berücksichtigung ihrer Wechselwirkung*. Technische Universität Hamburg-Harburg, 1964.

[25] L.W. Ward. “The xy method of determination of ship wave resistance from the wave pattern”. In: *International seminar on theoretical waveresistance* (1963).

[26] Lawrence W Ward. “Experimental determination of wave resistance of a ship model from lateral wave-slope measurements”. en. In: (1968).

[27] *WASP (Ecoliner) - Dykstra Naval Architects*. URL: https://www.dykstra-na.nl/designs/wasp-ecoliner/ (visited on 03/04/2026).

[28] David C. Wilcox. *Turbulence modeling for CFD*. en. 3rd ed. La Cãnada, Calif: DCW Industries, 2006. ISBN: 978-1-928729-08-2.

A

Longitudinal wave cut

In subsection 2.5.1, a transverse wave cut formula has been derived from a momentum analysis. This can also be done using a longitudinal wave cut, following the same pattern. For this case, the control volume block will be chosen so that momentum flux is only present at the side boundaries at starboard and port side. For this case, the sides are infinitely long in x-direction so that the wave pattern exits via the sides and not via the back plane. A schematic drawing can be seen in Figure A.1.

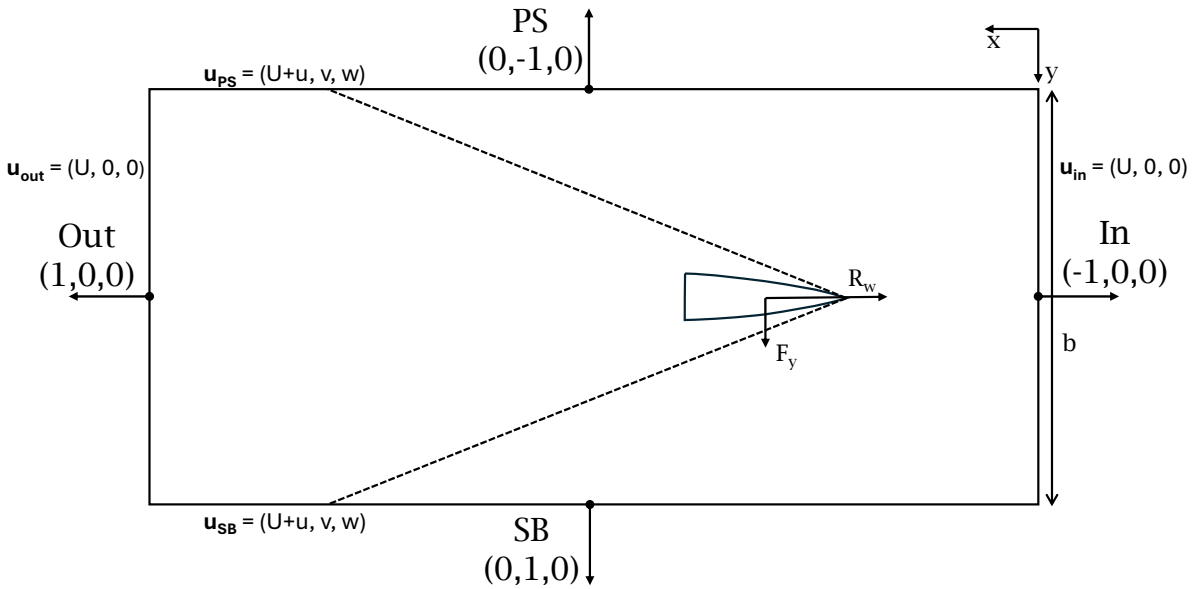

Figure A.1: Control volume for a longitudinal wave cut

Again the derivation starts with the (reduced) momentum equation for a fluid:

$$\oiint_{CS} \rho \mathbf{u}\mathbf{u} \cdot n \, dS = \oiint_{CS} \mathbf{t} \, dS \tag{A.1}$$

Start with calculating the left side of the equation for each plane. The top and bottom plane results in zero, the momentum flux in the in and out-plane is given by:

$$M_{in} = \left[\int_{-b/2}^{b/2} \int_{-h}^{0} \rho \begin{bmatrix} U \\ 0 \\ 0 \end{bmatrix} \begin{bmatrix} U \\ 0 \\ 0 \end{bmatrix} \cdot \begin{bmatrix} -1 \\ 0 \\ 0 \end{bmatrix} \, dz \, dy \right] \cdot \begin{bmatrix} 1 \\ 0 \\ 0 \end{bmatrix} = -\rho U^2 \cdot b \cdot h \tag{A.2}$$

$$M_{out} = \left[\int_{-b/2}^{b/2} \int_{-h}^{0} \rho \begin{bmatrix} U \\ 0 \\ 0 \end{bmatrix} \begin{bmatrix} U \\ 0 \\ 0 \end{bmatrix} \cdot \begin{bmatrix} 1 \\ 0 \\ 0 \end{bmatrix} \, dz \, dy \right] \cdot \begin{bmatrix} 1 \\ 0 \\ 0 \end{bmatrix} = \rho U^2 \cdot b \cdot h \tag{A.3}$$

These sum up to zero. For the SB, the momentum flux can be calculated as:

$$M_{SB} = \left[\int_{-\infty}^{\infty} \int_{-h}^{\zeta_{SB}} \rho \begin{bmatrix} U+u \\ v \\ w \end{bmatrix} \begin{bmatrix} U+u \\ v \\ w \end{bmatrix} \cdot \begin{bmatrix} 0 \\ 1 \\ 0 \end{bmatrix} \, dz \, dy \right] \cdot \begin{bmatrix} 1 \\ 0 \\ 0 \end{bmatrix} = \rho \int_{-\infty}^{\infty} \int_{-h}^{\zeta_{SB}} (U + u_{SB}) v_{SB} \, dz \, dx \tag{A.4}$$

Following the same steps for the PS plane, it results in:

$$M_{PS} = -\rho \int_{-\infty}^{\infty} \int_{-h}^{\zeta_{PS}} (U + u_{PS}) v_{PS} \, dz \, dx \tag{A.5}$$

Now the right side of Equation A.1 can be derived. The SB, PS, top and bottom plane have no contribution on the control volume, as $\hat{n} \cdot \hat{x} = 0$. The contribution of the in and out plane are:

$$F_{in} = \int_{-\infty}^{\infty} \int_{-h}^{0} p_{in} \cdot \hat{n} \, dz \, dx \tag{A.6}$$

$$F_{out} = \int_{-\infty}^{\infty} \int_{-h}^{0} p_{out} \cdot \hat{n} \, dz \, dx \tag{A.7}$$

$p_{in} = p_{out}$, so this results in a net contribution of zero. The only contribution is the force from the hull (R_w). Equation A.1 can now be filled in. This results in the following expression for the wave resistance.

$$R_w = \rho \int_{-\infty}^{\infty} \int_{-h}^{\zeta_{PS}} (U + u_{PS}) v_{PS} \, dz \, dx - \rho \int_{-\infty}^{\infty} \int_{-h}^{\zeta_{SB}} (U + u_{SB}) v_{SB} \, dz \, dx \tag{A.8}$$

$$= \rho \int_{-\infty}^{\infty} \int_{-h}^{\zeta_{PS}} U v_{PS} + u_{PS} v_{PS} \, dz \, dx - \rho \int_{-\infty}^{\infty} \int_{-h}^{\zeta_{SB}} U v_{SB} + u_{SB} v_{SB} \, dz \, dx \tag{A.9}$$

Conservation of mass gives:

$$\rho \int_{-\infty}^{\infty} \int_{-h}^{\zeta_{PS}} v_{PS} \, dz \, dx - \rho \int_{-\infty}^{\infty} \int_{-h}^{\zeta_{SB}} v_{SB} \, dz \, dx = 0 \tag{A.10}$$

Substituting this in Equation A.8 gives:

$$R_w = \rho \int_{-\infty}^{\infty} \int_{-h}^{\zeta_{PS}} u_{PS} v_{PS} \, dz \, dx - \rho \int_{-\infty}^{\infty} \int_{-h}^{\zeta_{SB}} u_{SB} v_{SB} \, dz \, dx \tag{A.11}$$

This expression is valid for asymmetric flows. In that case, a longitudinal wave cut on each side of the ship is needed. When the flow is symmetric, the result reduces to Equation A.12. In this case $u_{SB} = u_{PS}$ and $v_{SB} = -v_{PS}$ and only one wave cut is needed.

$$\boxed{R_w = 2\rho \int_{-\infty}^{\infty} \int_{-h}^{\zeta} uv \, dz \, dx} \tag{A.12}$$

B

Transformation of the wave resistance formula

This appendix will show that the wave resistance formula from the transverse wave cut of Equation 3.18 is similar to the one Havelock presented [7]. Therefore, the wave resistance formula should be rewritten from the transverse wave number (u) domain to the θ domain. As shown, the wave resistance formula presented by Eggers et al. [5] is given as:

$$R_w = \frac{1}{16\pi} \int_{-\infty}^{\infty} \left[F^2(u) + G^2(u)\right] \frac{\sqrt{1+4u^2}}{1+\sqrt{1+4u^2}}\, du \tag{B.1}$$

Using $u = \tan(\theta)\sec(\theta)$, gives:

$$\frac{du}{d\theta} = \frac{1+\sin^2(\theta)}{\cos^3(\theta)} \tag{B.2}$$

$$du = \frac{1+\sin^2(\theta)}{\cos^3(\theta)} d\theta \tag{B.3}$$

We can use this to convert du to $d\theta$. For converting $G(u)$ and $F(u)$ to the θ domain, the following relation can be used.

$$G(u) + iF(u) = \frac{4\pi\cos^3(\theta)}{1+\sin^2(\theta)}[g(\theta) + if(\theta)] \tag{B.4}$$

$$G^2(u) + F^2(u) = \frac{16\pi^2\cos^6(\theta)}{(1+\sin^2(\theta))^2}[g^2(\theta) + f^2(\theta)] \tag{B.5}$$

Now only $\frac{\sqrt{1+4u^2}}{1+\sqrt{1+4u^2}}$ is left in the integral. A different way or writing u is $u = \frac{\sin(\theta)}{\cos^2(\theta)}$. Substituting this in $\sqrt{1+4u^2}$ gives:

$$\sqrt{1+4u^2} = \sqrt{1+4\frac{\sin^2(\theta)}{\cos^4(\theta)}} = \frac{\sqrt{\cos^4(\theta)+4\sin^2(\theta)}}{\cos^2(\theta)} \tag{B.6}$$

Using the Pythagorean identity $\cos^2(\theta) = 1 - \sin^2(\theta)$ and simplifying gives the following:

$$\sqrt{1+4u^2} = \frac{1+\sin^2(\theta)}{\cos(\theta)} \tag{B.7}$$

Inserting this in $\frac{\sqrt{1+4u^2}}{1+\sqrt{1+4u^2}}$ gives:

$$\frac{\sqrt{1+4u^2}}{1+\sqrt{1+4u^2}} = \frac{1+\sin^2(\theta)}{2} \tag{B.8}$$

Now that all parts of the integral have been sorted, it can be substituted in Equation B.1.

$$R_w = \frac{1}{16\pi}\int_{-\infty}^{\infty}[g^2(\theta)+f^2(\theta)]\frac{16\pi^2\cos^6(\theta)}{(1+\sin^2(\theta))^2}\frac{1+\sin^2(\theta)}{2}\frac{1+\sin^2(\theta)}{\cos^3(\theta)}d\theta \tag{B.9}$$

$$= \frac{\pi}{2}\int_{-\frac{\pi}{2}}^{\frac{\pi}{2}}[g^2(\theta)+f^2(\theta)]\cos^3(\theta)\,d\theta \tag{B.10}$$

This result is indeed the same as the result Havelock obtained. Only difference is in the scaling, as this expression is non-dimensional. This shows the equivalence between the angular and transverse wave number formulations of the wave resistance.

C

Rewrite Side force formula

$$F_y = \frac{\pi}{2} \int_{-\frac{\pi}{2}}^{\frac{\pi}{2}} [g^2(\theta) + f^2(\theta)] \cos^2(\theta) \sin(\theta)\, d\theta \tag{C.1}$$

Using $u = \tan(\theta)\sec(\theta)$, gives:

$$d\theta = \frac{\cos^3(\theta)}{1 + \sin^2(\theta)} du \tag{C.2}$$

From Eggers et al. (1967)[5], the following relation can be found.

$$G(u) + iF(u) = \frac{4\pi \cos^3(\theta)}{1 + \sin^2(\theta)} [g(\theta) + if(\theta)] \tag{C.3}$$

$$g^2(\theta) + f^2(\theta) = \frac{(1 + \sin^2(\theta))^2}{16\pi^2 \cos^6(\theta)} [G^2(u) + F^2(u)] \tag{C.4}$$

Substituting this in Equation C.1, gives:

$$F_y = \frac{\pi}{2} \int_{-\frac{\pi}{2}}^{\frac{\pi}{2}} [G^2(u) + F^2(u)] \frac{(1 + \sin^2(\theta))^2}{16\pi^2 \cos^6(\theta)} \cos^2(\theta) \sin(\theta) \frac{\cos^3(\theta)}{1 + \sin^2(\theta)}\, du \tag{C.5}$$

$$= \frac{1}{32\pi} \int_{-\infty}^{\infty} [G^2(u) + F^2(u)](1 + \sin^2(\theta)) \tan(\theta)\, du \tag{C.6}$$

In Appendix B, the following relation between u and θ was derived, which can be used again.

$$\frac{\sqrt{1 + 4u^2}}{1 + \sqrt{1 + 4u^2}} = \frac{1 + \sin^2(\theta)}{2} \tag{C.7}$$

Rewriting gives:

$$(1 + \sin^2(\theta)) \tan(\theta) = 2 \frac{\sqrt{1 + 4u^2}}{1 + \sqrt{1 + 4u^2}} \tan(\theta) \tag{C.8}$$

$u = \tan(\theta)\sec(\theta)$ and $s = \sec(\theta)$ can be used to remove $\tan(\theta)$ from the right side from the equation.

$$\frac{u}{s} = \tan(\theta) \tag{C.9}$$

And using the relation between u and s:

$$s(u) = \sqrt{\frac{1 + \sqrt{1 + 4u^2}}{2}} \tag{C.10}$$

$(1+\sin^2(\theta))\tan(\theta)$ then becomes:

$$2u\frac{\sqrt{1+4u^2}}{1+\sqrt{1+4u^2}}\sqrt{\frac{2}{1+\sqrt{1+4u^2}}} \tag{C.11}$$

Filling this in the F_y-equation, it can be found that the side force in terms of transverse wave number n is given as:

$$F_y = \frac{1}{16\pi}\int_{-\infty}^{\infty}[F^2(u)+G^2(u)]\frac{u\sqrt{1+4u^2}}{1+\sqrt{1+4u^2}}\sqrt{\frac{2}{1+\sqrt{1+4u^2}}}\,du \tag{C.12}$$

D

Side force integral results

Results for the side force integral form will be presented here. The equation below describes the integral used to obtain the side force from flow data in a transverse plane behind the ship. The Neumann-Kelvin panel method has been used to simulate the flow. The results of wave pattern analysis do not correspond to the results from pressure integration. It has not been found out why this is the case. The side force results for varying longitudinal location, mesh size, angle, and velocity are shown in the figures below.

$$F_y = \rho \int_{-b/2}^{b/2} \int_{-h}^{\zeta} (U + \phi_x)\phi_y \, dz \, dy \tag{D.1}$$

Longitudinal position of TWC

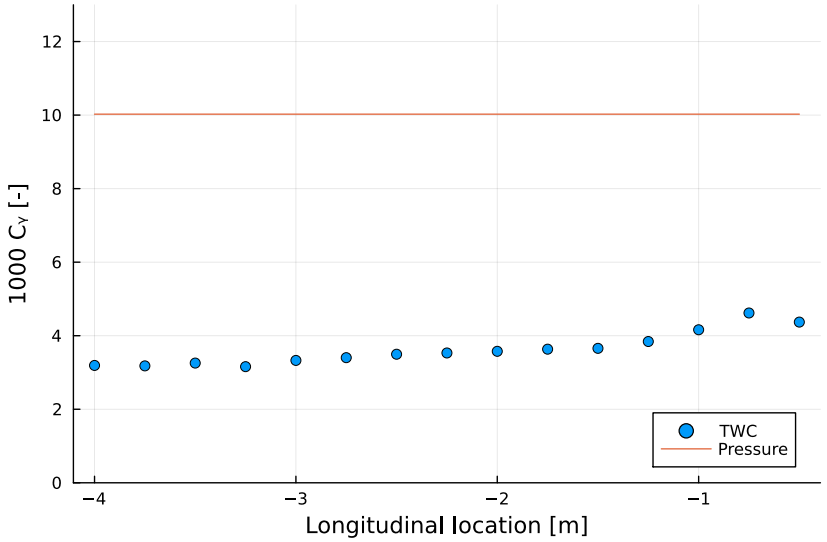

Figure D.1: Side force for different longitudinal position of the TWC

Grid convergence

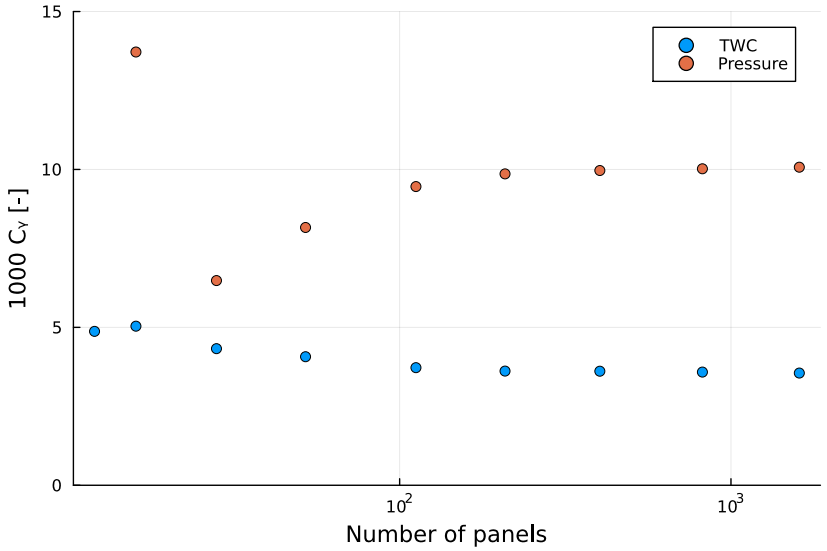

Figure D.2: Side force for different panel sizes

Angle

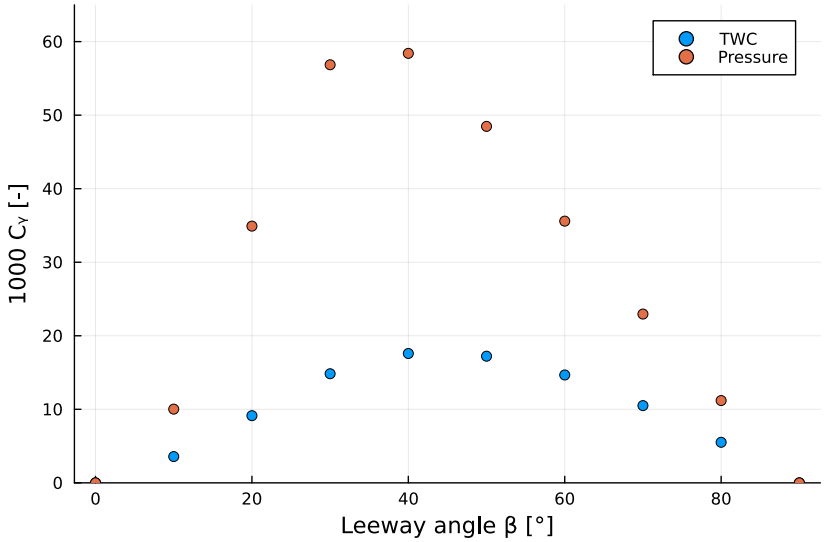

Figure D.3: Side force for different leeway angles

Velocity

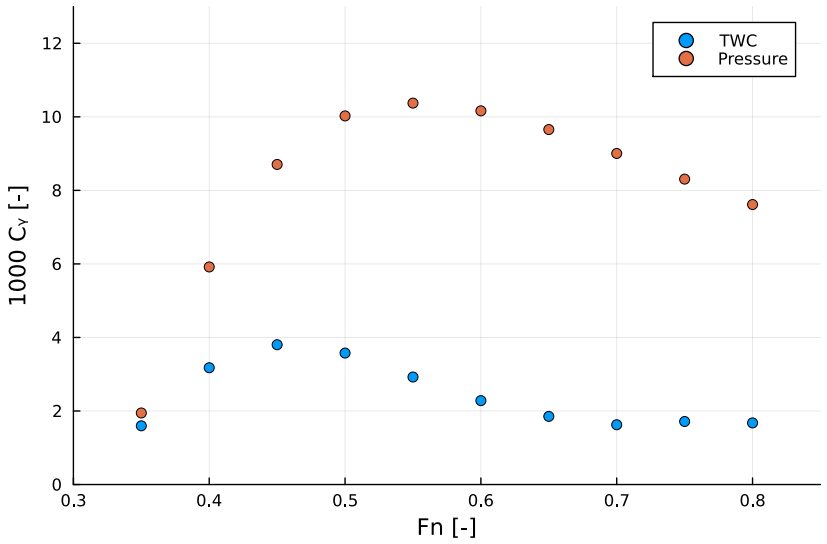

Figure D.4: Side force for different panel sizes